Dai *et al. Human Genomics* (2026) 20:93
https://doi.org/10.1186/s40246-026-00982-3

Human Genomics

RESEARCH Open Access

Integrating single-cell multi-omics and machine learning to reveal triaptosis heterogeneity in clear cell renal cell carcinoma

Haojie Dai[1,2†], Renjun Lu[1,2,3†], Mingcong Zhang[4†], Zhenyu Hang[1], Ke Jiang[1], Chao Qin[1,2,3*] and You Zhao[1*]

Abstract

Triaptosis, an emerging form of cell death, remains poorly characterized in terms of its heterogeneity within clear cell renal cell carcinoma (ccRCC). Utilizing single-cell transcriptomics, we delineate a landscape of triaptosis heterogeneity and identify monocytes and macrophages as exhibiting the highest triaptosis activity, which further increases upon terminal differentiation. These high-activity cells also demonstrate enhanced pro-angiogenic signaling toward endothelial cells. Within epithelial cells, subpopulations with the strongest triaptosis activity are located at the late differentiation stage and are closely associated with ccRCC traits. Spatial transcriptomic analysis reveals a decline in triaptosis activity with increasing distance from the tumor epithelial core. The epithelial cluster with the highest triaptosis activity showed reduced metabolic activity. In bulk transcriptome analysis, patients with high epithelial triaptosis activity infiltration exhibited improved prognosis, broader immune activation, and similarly suppressed metabolism. We subsequently developed a robust 4-gene prognostic signature based on module genes derived from high-triaptosis epithelial subpopulations. This model showed strong performance in prognostic stratification, immunotherapy guidance, and chemotherapy response prediction. Finally, we identified SLC25A37 as a core oncogenic gene within the signature and proposed Yohimbic acid among several potential molecularly targeted therapeutics.

Keywords Triaptosis, Clear cell renal cell carcinoma, Single cell, Prognosis

Introduction

Renal cell carcinoma (RCC) accounts for nearly 500,000 new cases each year worldwide [1], making it the sixth most commonly diagnosed cancer globally [2]. The clear cell subtype (ccRCC) represents the predominant form of RCC, comprising more than 70% of all cases [1]. While localized disease is associated with favorable outcomes, with 5-year survival rates approaching 95% [3], significant clinical challenges remain due to the marked clinicopathological heterogeneity of the disease [4]. Notably, metastases are either detected at initial diagnosis or develop during follow-up in approximately 30% of ccRCC patients [5], leading to poor prognosis and 5-year survival rates of less than 10% [6]. Thus, there is a pressing

†Haojie Dai, Renjun Lu and Mingcong Zhang have contributed equally to this work.

*Correspondence:
Chao Qin
Qinc_uro@163.com
You Zhao
zhaoyou0183@163.com
[1]The Affiliated Liyang People's Hospital of Kangda College of Nanjing Medical University, Liyang Branch Hospital of Jiangsu Province Hospital, Liyang, Changzhou, Jiangsu, China
[2]The First Clinical Medical College, Nanjing Medical University, Nanjing, Jiangsu, China
[3]Department of Urology, The First Affiliated Hospital of Nanjing Medical University, Nanjing Medical University, Nanjing, Jiangsu, China
[4]Department of Urology, The Second People's Hospital of Lianyungang, Affiliated Lianyungang Clinical College of Nantong University, Lianyungang, Jiangsu, China

need to identify reliable biomarkers to support clinical decision-making, facilitate accurate prognostic stratification, guide targeted therapies, and elucidate mechanisms underlying tumor development and progression.

Programmed cell death is a tightly governed biological process mediated by specific biomolecules, which stands in fundamental contrast to accidental cell death [7–8]. Dysregulation of this programmed mechanism is strongly implicated in the initiation and advancement of cancer [9]. Recently, since its debut in Science in October 2024, an emerging cell death mode known as triaptosis has come to the attention of scientists. Menadione, a fat-soluble precursor of vitamin K, triggers a distinct form of cell death known as triaptosis through oxidative modification of phosphatidylinositol 3-kinase PIK3C3/VPS34. Specifically, it depletes glutathione (GSH) and promotes reactive oxygen species (ROS) generation, leading to the oxidation of cysteine residues (Cys54 and Cys61) on PIK3C3. This oxidative event results in a reduction of phosphatidylinositol 3-phosphate (PI(3)P), subsequent endosomal dysfunction, and ultimately the induction of triaptosis, illustrating how excessive oxidative stress disrupts organellar integrity and activates specific cell death pathways [10–11]. However, the heterogeneity of triaptosis within the ccRCC microenvironment remains largely unknown, and the role of triaptosis activity in regulating key biological functions of ccRCC warrants further investigation.

In this study, we first analyzed triaptosis heterogeneity in monocytes and macrophages—the cell populations exhibiting the strongest triaptosis activity—based on single-cell omics data. Subsequently, focusing on epithelial cells as representative cancer cells, we identified the subpopulations with the highest triaptosis activity, meticulously dissected their metabolic and functional landscapes, and mapped their characteristics onto spatial and bulk transcriptomes to further explore their identity. Finally, recognizing the prognostic relevance of this highly triaptotic epithelial cell population, we extracted its representative genes and integrated ten machine learning algorithms to construct a prognostic risk model. This advanced clinical progress in prognosis stratification, immunotherapy efficacy prediction, and chemotherapy sensitivity prediction. Furthermore, we developed molecularly targeted drugs based on the model's core oncogene. In summary, our integration of multi-omics and machine learning advances the exploration of triaptosis heterogeneity in ccRCC, bridges biological and clinical disparities and fills the gap in this field.

Materials and methods

Data acquisition

The single-cell dataset GES171306 [12] for ccRCC was acquired from the TISCH2 portal (http://tisch.compbio.cn/home/) and comprises two bilateral sporadic tumor samples. GWAS data for RCC were sourced from the IEU OpenGWAS project (https://gwas.mrcieu.ac.uk/). Spatial transcriptomics data (sample accession: GSM5924033 [13]) and bulk transcriptomics cohort GSE167573 [14] for ccRCC were downloaded from the GEO database. The TCGA-KIRC cohort, representing bulk transcriptomics data for ccRCC, was obtained from UCSC Xena, while the E-MTAB-1980 dataset was retrieved from the ArrayExpress database. Additionally, the ccRCC immunotherapy cohort published by Braun et al. was accessed via the supplementary materials of the corresponding Nature Medicine article [15]. Triaptosis-related genes were obtained from previous article [16].

Comprehensive single-cell analysis process

Single-cell analysis primarily relies on Seurat V5. For certain algorithms requiring V4 data structures, we employed the scCustomize package for conversion. After constructing single-cell files using CreateSeuratObject, we performed quality control based on thresholds: total number of molecules detected within a cell > 1000, number of genes detected in each cell between 200 and 10,000, and mitochondrial gene proportion ≤ 20%. Following data normalization with NormalizeData, we extracted highly variable genes using FindVariableFeatures and performed PCA dimensionality reduction after data normalization. Subsequently, RunHarmony removed batch effects between samples, selected optimal clustering parameters, and visualized results via UMAP dimensionality reduction. We annotated distinct cell populations—particularly monocytes and macrophages—based on classical cellular markers from prior literature [17–18]. This completes the fundamental preparation of single-cell data.

Cell activity scores based on gene sets are computed using the AUCell algorithm, while cell-cell receptor communication analysis utilizes the CellChat package. Cell differentiation potential is assessed via the CytoTRACE package, and pseudo-timing is generated using the Monocle 3 package. The scPagwas package bridges single-cell omics with GWAS data to compute trait-associated scores for each cell [19]. Additionally, metabolic activity in single-cell transcriptomes was assessed using the scMetabolism package. Mapping single-cell transcriptomic data to bulk transcriptomes was performed via the BayesPrism package to obtain cell infiltration scores for each sample [20]. The hdWGCNA package successfully mitigated sparsity in single-cell transcriptomes, enabling weighted gene co-expression network analysis (WGCNA) across cells to extract representative module genes.

Spatial transcriptomics analysis

Spatial transcriptomics data were read using Seurat V5. Additionally, spatial transcriptomics data were deconvoluted using the Robust Cell Type Decomposition (RCTD) algorithm based on the spacexr package [21]. The GetTissueCoordinates function was employed to obtain coordinates for each spatial spot, thereby calculating the tumor epithelial core location.

Machine learning prognostic model development

Based on key module genes identified by hdWGCNA, we sequentially employed univariate Cox regression and Lasso regression to screen genes closely associated with prognosis. Subsequently, drawing upon Liu et al.'s machine learning modeling approach [22], we integrated Random Survival Forest (RSF), Elastic Network (Enet), Lasso, Ridge, stepwise Cox, CoxBoost, partial least squares regression for Cox (plsRcox), supervised principal components (SuperPC), generalized boosted regression modeling (GBM), and survival support vector machine (survival-SVM) to construct the optimal prognostic model. The TCGA-KIRC cohort served as the training set, while E-MTAB-1980 and GSE167573 were used as validation sets. The combination yielding the highest average C-index was deemed to possess the greatest prognostic guidance potential. Additionally, for black-box model explanation, we employed SurvSHAP(t) from survex R package [23]. This algorithm, derived from SHAP explanation, links the contribution of variables in black-box survival models to outcome predictions with survival time, advancing the credibility and transparency of artificial intelligence in clinical practice.

Immune infiltration and functional activation landscape analysis

The stromal score and immune score were assessed using the Estimate package, while the specific immune cell infiltration was obtained via the CIBERSORT algorithm [24]. Additionally, multiple immune function-related gene sets were acquired from the ImmPort database (https://www.immport.org/shared/home). Differentially expressed genes in single-cell omics were identified using the FindAllMarkers function with thresholds of padj < 0.05 and logFC > 0.25. In bulk transcriptomics, differentially expressed genes were extracted using the limma package with thresholds of padj < 0.05 and logFC > 1. Subsequent enrichment analysis based on GO and KEGG was performed using the clusterProfiler package. Additionally, functional scoring of multiple gene sets was performed using the ssGSEA algorithm.

Chemotherapy sensitivity analysis and targeted drug screening

Using the oncoPredict package, we integrated GDSC2 data to assess the sensitivity of TCGA-KIRC cohort patients to 198 chemotherapy drugs, measured by IC50. Additionally, we conducted an in-depth analysis of the PRISM and CTRP databases using the "pRRophetic" package, focusing on the AUC of drug response, and screened drugs with significant negative correlations with TES based on Spearman correlation analysis to identify potential chemotherapy regimens with high TES.

Following the prediction of small molecule drugs targeting core genes via the DSigDB database within the Enrichr platform, the corresponding protein and compound structures were retrieved from the AlphaFold and PubChem. Molecular docking was performed with AutoDock 4.2 and AutoDock Tools 1.5.7 after preparing the protein structures through removal of crystallographic water molecules, addition of hydrogen atoms, and assignment of charge parameters. The resulting docked complexes were visualized using PyMOL 3.0.5.

Molecular dynamics (MD) simulations were conducted in Gromacs 2022. Force field parameters were assigned using pdb2gmx and the AutoFF web server, with the CHARMM36 force field applied to the protein and the CGenff force field to the ligand. The system was solvated in a cubic box of TIP3P water molecules with a 1 nm buffer zone around the solute, and counterions were added with gmx genion to neutralize the system. Long-range electrostatic interactions were computed using the Particle Mesh Ewald (PME) method with a 1.0 nm cutoff, and the SHAKE algorithm was employed to constrain covalent bonds. Equations of motion were integrated with the Verlet leapfrog algorithm using a 1-fs time step. Energy minimization proceeded in three stages: (1) 3,000 steps of steepest descent with restrained solute atoms (water minimization), (2) 2,000 steps of conjugate gradient with restrained counterions, and (3) unconstrained minimization of the entire system. Production simulation was carried out in the NPT ensemble at 310 K for 100 ns. Trajectory analysis included calculations of root-mean-square deviation (RMSD; gmx rms), root-mean-square fluctuation (RMSF; gmx rmsf), hydrogen bonding (gmx hbond), radius of gyration (Rg; gmx gyrate), and solvent-accessible surface area (SASA; gmx sasa). Binding free energies were estimated using the MM-PBSA approach with g_mmpbsa.

Quantitative real-time PCR (qRT-PCR)

The specific methods for total RNA extraction and qRT-PCR are described in supplementary materials. The following primers were used in this study:

RORA forward, 5'-CTTGCCGTAGGGATGTCTCG-3' and.

RORA reverse, 5'-GAAGTTCCGTCAGCCCGTT-3';
PKHD1 forward, 5'-GGACCACGAGATAGCTGTAC T-3' and.
PKHD1 reverse, 5'-CCCATTTGTCTCCTTGAGCT T-3';
SLC25A37 forward, 5'-AGAAAATCATGCGGACCGA AG-3' and.
SLC25A37 reverse, 5'-TGGTGGTGGAAAACGTCAT TTA-3';
PNISR forward, 5'-ATGTGGGATCAAGGAGGACA G-3' and.
PNISR reverse, 5'-CAGCCCAATCAATCTGGCTT-3';
Actin forward, 5'-GAAGATCAAGATCATTGCTCCT C-3' and.
Actin reverse, 5'-ATCCACATCTGCTGGAAGG-3'.

Actin was used as an internal control. The procedures were performed three times to ensure accuracy and precision. The relative expression levels were calculated using the $2^{-\Delta\Delta CT}$ method. Immunohistochemical images for the gene were sourced from The Human Protein Atlas, comparing both cancerous and non-cancerous renal tissues.

Statistical analysis

All statistical analyses and data visualization were conducted using R (version 4.4.1). A significance threshold of $P < 0.05$ was adopted, with multiple testing corrections performed using the Benjamini–Hochberg method to control the false discovery rate (FDR) where applicable. Inter-group differences were assessed primarily with the Wilcoxon rank-sum test, and correlations were evaluated using Spearman's rank-based method.

Results

Triaptosis in the ccRCC microenvironment, with a focus on monocytes and macrophages

Based on the GSE171306 ccRCC single-cell transcriptomics dataset, we clustered 24 clusters (Fig. 1A) and annotated them into 10 cell types (Fig. 1B, Fig S1). We calculated the triaptosis activity of each cell using the AUCell algorithm and found that monocytes and macrophages had the highest scores (Fig. 1C-D). We then focused on these two cell types and extracted them for detailed analysis. The Monocyte/Macrophage cell population was further clustered into 7 clusters (Fig. 1E), with clusters 3 and 4 representing monocytes and the remaining clusters representing macrophages (Fig. 1F, Fig S2). Cluster 3 exhibited non-classical monocyte characteristics, while cluster 4 was VCAN-positive. Clusters 0–2 represent typical inflammatory macrophages, with cluster 0 highly expressing CLDN1 and cluster 1 highly expressing LILRB5. Cluster 5, which highly expresses AREG, is considered to have more pronounced angiogenic characteristics, while cluster 6, which expresses COL5A2, is considered to be associated with the matrix. Overall, the Mono/Macro cell population exhibits nearly identical high triaptosis activity (Fig. 1G-H). CytoTRACE was used to assess the differentiation potential of cell clusters (Fig. 1I-J). Interestingly, when focusing on the entire Mono/Macro cell population, we found that cells with lower differentiation potential exhibited higher triaptosis activity (Fig. 1K-L). We then evaluated cell communication in Mono/Macro cells with high and low triaptosis activity. We found that Mono/Macro cells with high triaptosis activity exhibit stronger intercellular connections with endothelial cells (Fig. 1M), particularly in terms of vascular endothelial growth factor (VEGF) receptor-mediated signaling (Fig. 1N-O). Additionally, low triaptosis activity macrophages exhibit SPP1-mediated cell-to-cell communication with endothelial cells, whereas this is absent in high triaptosis activity macrophages.

The landscape of triaptosis in epithelial cells (malignant)

The authors who uploaded the GSE131076 raw data used InferCNV to determine that all epithelial cells in the sample were malignant cells, which is consistent with the fact that ccRCC is a cancer derived from renal tubular epithelium. We then focused on this group of epithelial cells to explore the triaptosis heterogeneity of the cancer cells themselves. The epithelial cells were extracted and divided into six groups (Fig. 2A-B), with Epi 6 exhibiting the strongest triaptosis activity (Fig. 2C-D). CytoTRACE analysis indicated that Epi 6 had the lowest differentiation potential (Fig. 2E-F), and pseudo-time analysis confirmed that Epi 6 was at the terminal stage of differentiation (Fig. 2G). This aligns with the previous finding that triaptosis activity was enriched in cells with low differentiation potential in the Mono/Macro group. Epithelial cells with high and low triaptosis activity exhibited similar cellular communication (Fig. 2H), though high triaptosis epithelial cells showed slightly enhanced vascular endothelial growth factor receptor interaction with endothelial cells. Additionally, low triaptosis epithelials exhibit PLG-mediated cell communication, which is absent in high triaptosis epithelial cells (Fig. 2I). We then utilized the scPagwas algorithm to link single-cell data with GWAS trait data, finding that in epithelial cells, the Epi 6 subpopulation with high triaptosis activity shows the highest association with renal cell carcinoma traits (Fig. 2J-K).

We then deconvoluted the single-cell data into the spatial transcriptome (Fig. 3A). Interestingly, the deconvolution algorithm determined that nearly all epithelial cells in the pathological sample exhibited high triaptosis activity (Fig. 3B). Based on this, we found that triaptosis activity decreased with increasing distance from the tumor

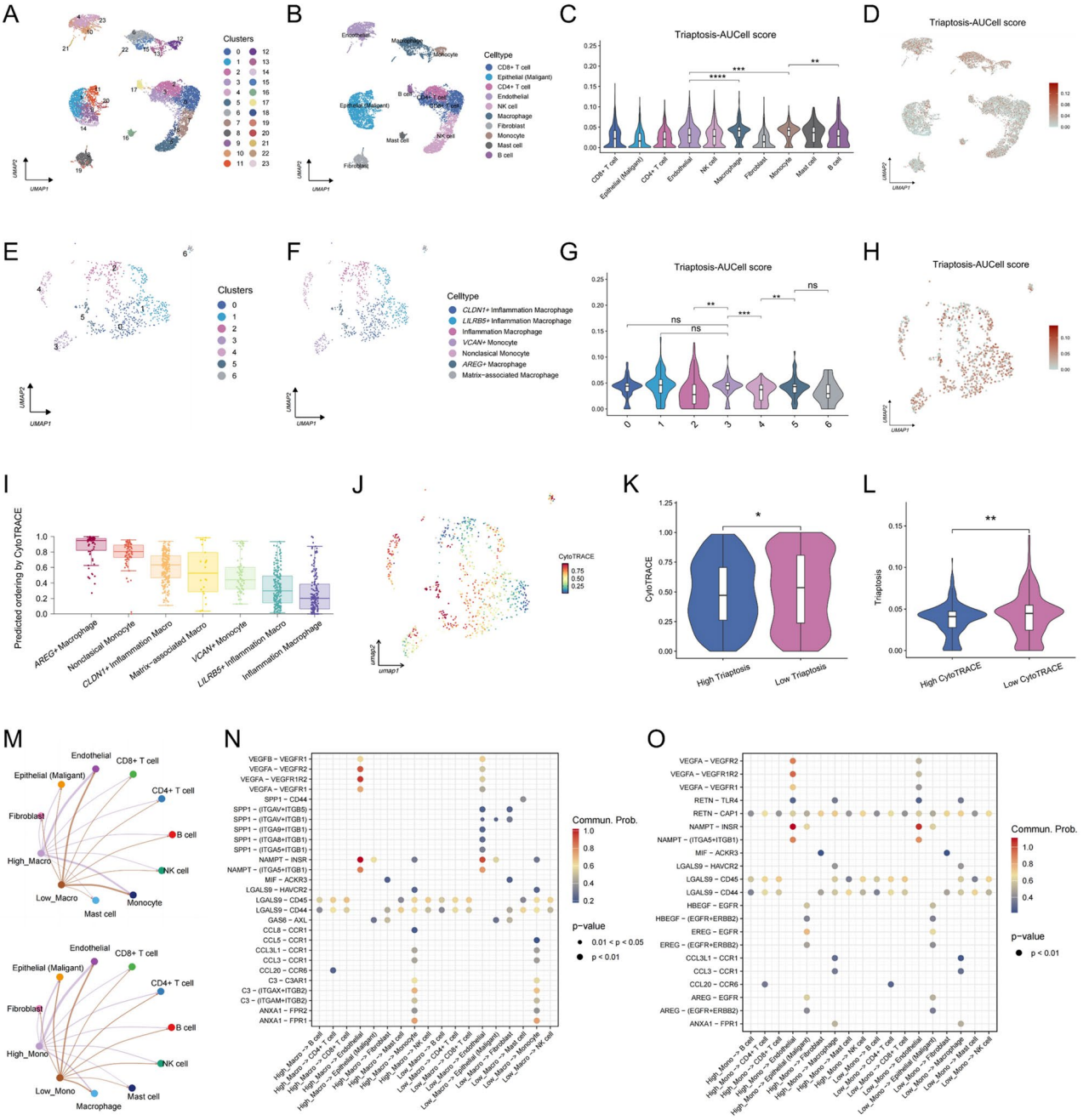

Fig. 1 The triaptosis landscape in the ccRCC microenvironment, focusing on monocyte-derived macrophages (**A**) Clusters of GSE171306 (**B**) Cell types of GSE171306 (**C**) Differences in triaptosis activity across various cell types (**D**) Landscape of triaptosis activity (**E**) Clusters of monocytes and macrophages (**F**) Subtypes of Mono/Macro cell populations (**G**) Differences in triaptosis activity in Mono/Macro (**H**) Landscape of triaptosis activity in Mono/Macro (**I**) Differences in CytoTRACE differentiation potential (**J**) Landscape of CytoTRACE differentiation potential (**K**) Differences in triaptosis activity between high and low CytoTRACE groups (**L**) Differences in differentiation potential between high and low triaptosis groups (**M**) Intercellular communication strength (**N**-**O**) Differences in cellular communication between macrophages (**N**) and monocytes (**O**) with high and low triaptosis activity

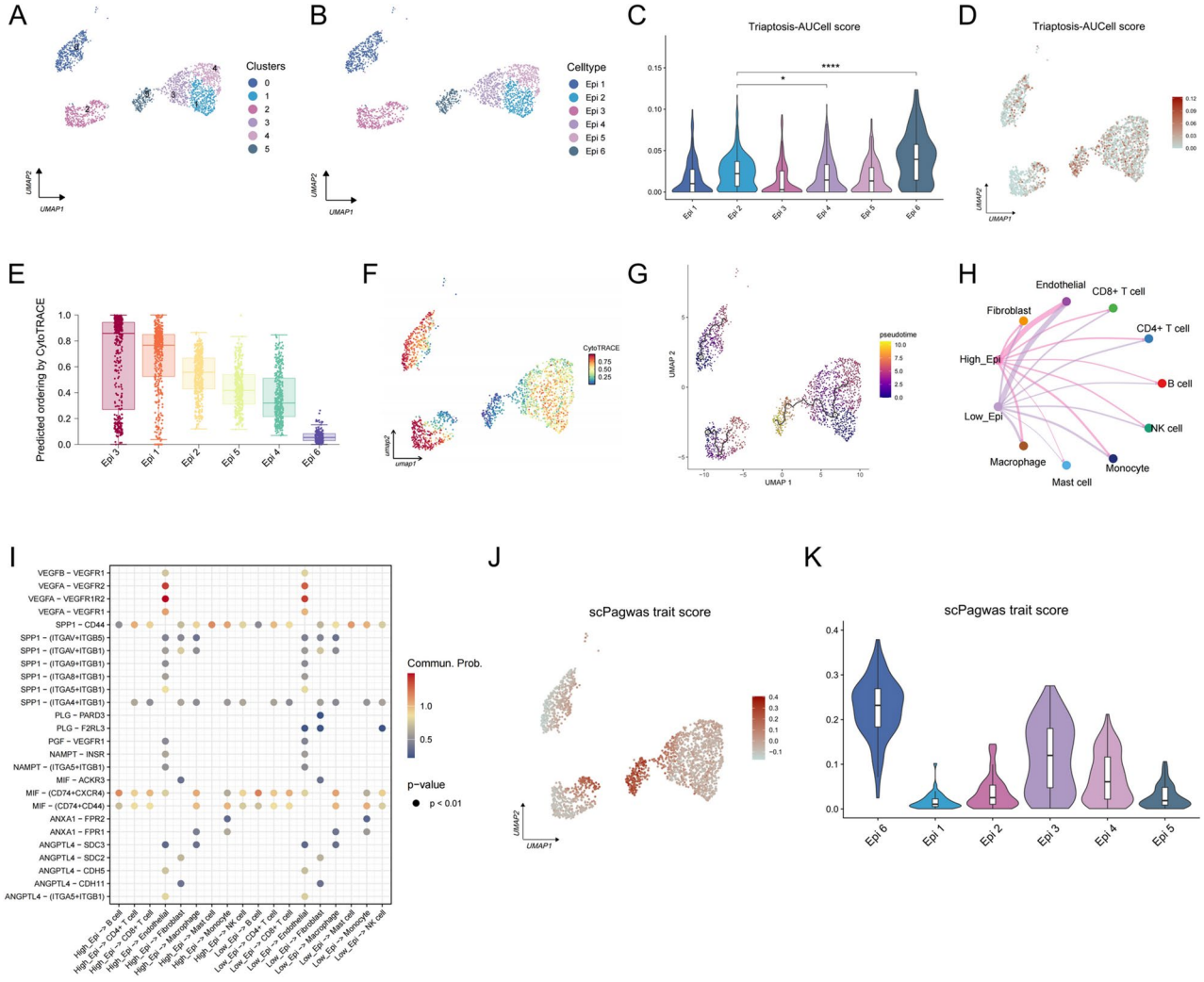

Fig. 2 The triaptosis landscape in epithelial (**A**) Clusters of epithelial (**B**) Subtypes of epithelial (**C**) Differences in triaptosis activity across epithelial types (**D**) Landscape of triaptosis activity (**E**) Differences in CytoTRACE differentiation potential (**F**) Landscape of CytoTRACE differentiation potential (**G**) Pseudotime sequence of epithelial cells (**H**) Intercellular communication strength (**I**) Differences in cellular communication between epithelials with high and low triaptosis activity (**J**) Landscape of scPagwas trait-related score (**K**) Differences in scPagwas trait-related score across epithelial types

core, indicating stronger triaptosis activity in the tumor core (Fig. 3C-D).

Metabolic and functional landscape of Epi 6 with high triaptosis activity

Given that Epi 6 exhibits the strongest triaptosis activity and is considered to be highly correlated with cancerous traits, we focused on this epithelial cell subpopulation for detailed analysis, with an emphasis on exploring metabolic and functional heterogeneity. In the three major metabolic pathways—glucose metabolism, lipid metabolism, and amino acid metabolism—Epi 6 showed significant downregulation (Fig. 4A). However, we observed significant upregulation in arginine biosynthesis (Fig. 4B-C) and glycerophospholipid metabolism (Fig. 4D-E). In some classic cancer-related functional pathways, oxidative phosphorylation and responses to oxidative stress were downregulated in Epi 6, while MAPK signaling, Hedgehog signaling and mTOR signaling were activated (Fig. 4F). Gene enrichment analysis of Epi 6-related differentially expressed genes highlighted dysregulation in transcription and translation processes within this cell population (Fig. 4G). Additionally, GSEA further emphasized the significant downregulation of oxidative phosphorylation (Fig. 4H).

Characteristics of Epi 6 infiltration at the bulk transcriptomic level

Utilizing the BayesPrism deconvolution algorithm, we projected the Epi 6 features at the single-cell transcriptomic level onto the bulk transcriptome, yielding the corresponding Epi 6 infiltration scores for each sample. During the deconvolution process, most ribosomal and mitochondrial genes were filtered out. Protein-coding

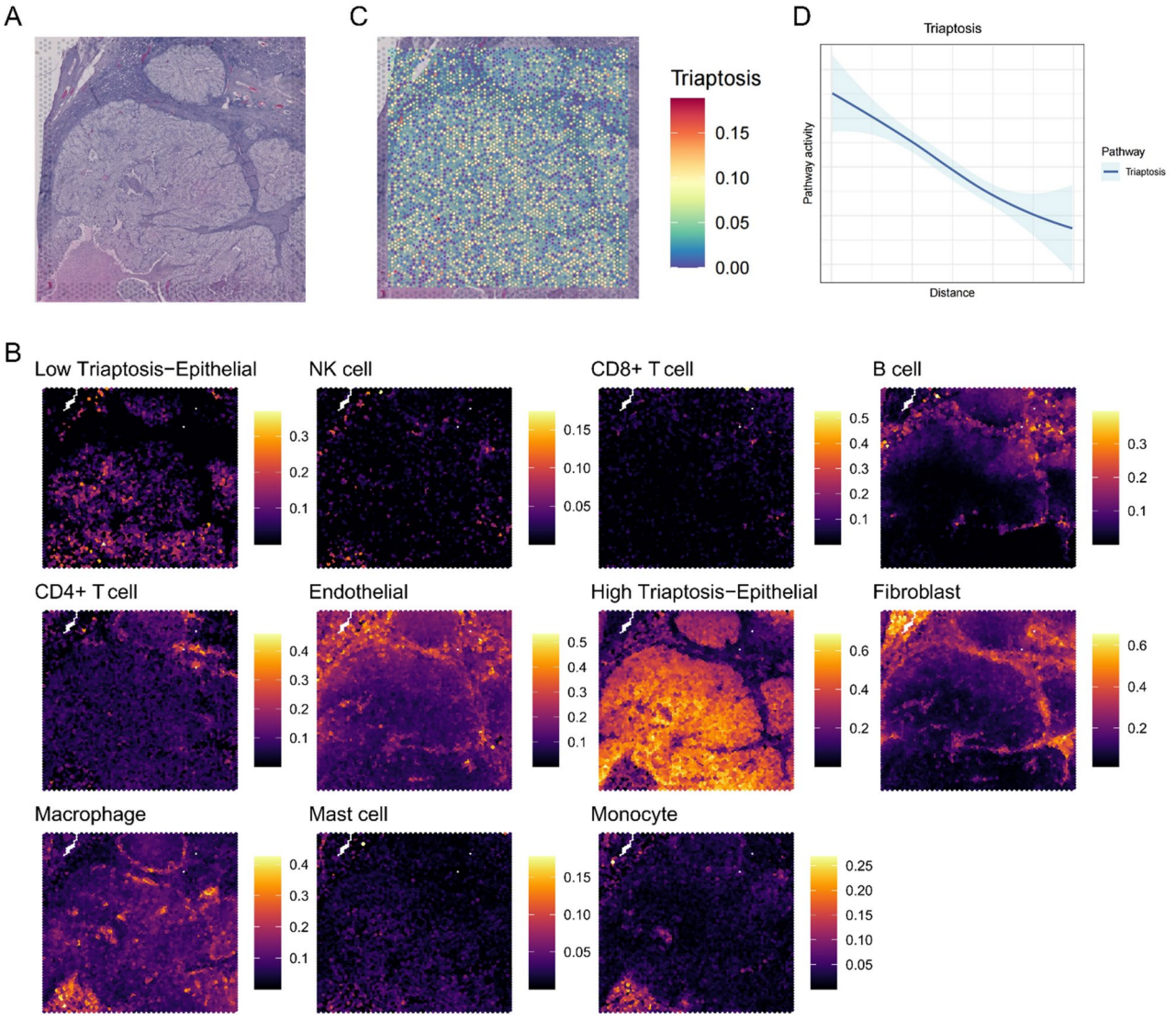

Fig. 3 Spatial Transcriptomic Landscape of Triaptosis (**A**) HE-stained section sample (**B**) Deconvolute single-cell transcriptomic cell types into spatial transcriptomics (**C**) Triaptosis activity in spatial transcriptomics (**D**) Triaptosis activity varies with distance from the tumor core

RNAs showed the highest correlation, whereas long non-coding RNAs and pseudogenes were largely not selected, indicating that the deconvolution primarily focused on protein-coding genes (Fig. 5A-B). Interestingly, the infiltration level of Epi 6 was lower in Stage III-IV patients compared to Stage I-II patients. Similarly, the infiltration of Epi 6 was also reduced in M1 patients compared to M0 patients (Fig. 5C). Additionally, we observed that patients with high Epi 6 infiltration exhibited longer overall survival, disease-specific survival, and progression-free interval (Fig. 5D). In summary, high Epi 6 infiltration with high triaptosis activity may be a characteristic of better prognosis in ccRCC.

Given this, we analyzed the functional activation landscape and immune differences between Epi 6 high- and low-infiltration subgroups. ssGSEA analysis based on the Hallmark gene set revealed that immune-related pathways were widely activated in the Epi 6 high-infiltration group, particularly interferon-related pathways and TNF-α signaling, while metabolic pathways were significantly downregulated, including but not limited to glycolysis, fatty acid metabolism, and ROS pathways (Fig. 5E). Additionally, we performed enrichment analysis on genes differing between the high- and low-infiltration subgroups, highlighting disruptions in pathways such as endothelial cell proliferation, the PI3K-AKT pathway, and the MAPK pathway (Fig. 5F).

We then conducted a detailed analysis of the immune landscape. Utilizing "Estimate", we observed that the high Epi 6 infiltration subgroup exhibited higher matrix scores and immune scores (Fig. 5G). Focusing on specific immune cells, we found that the high Epi 6 infiltration

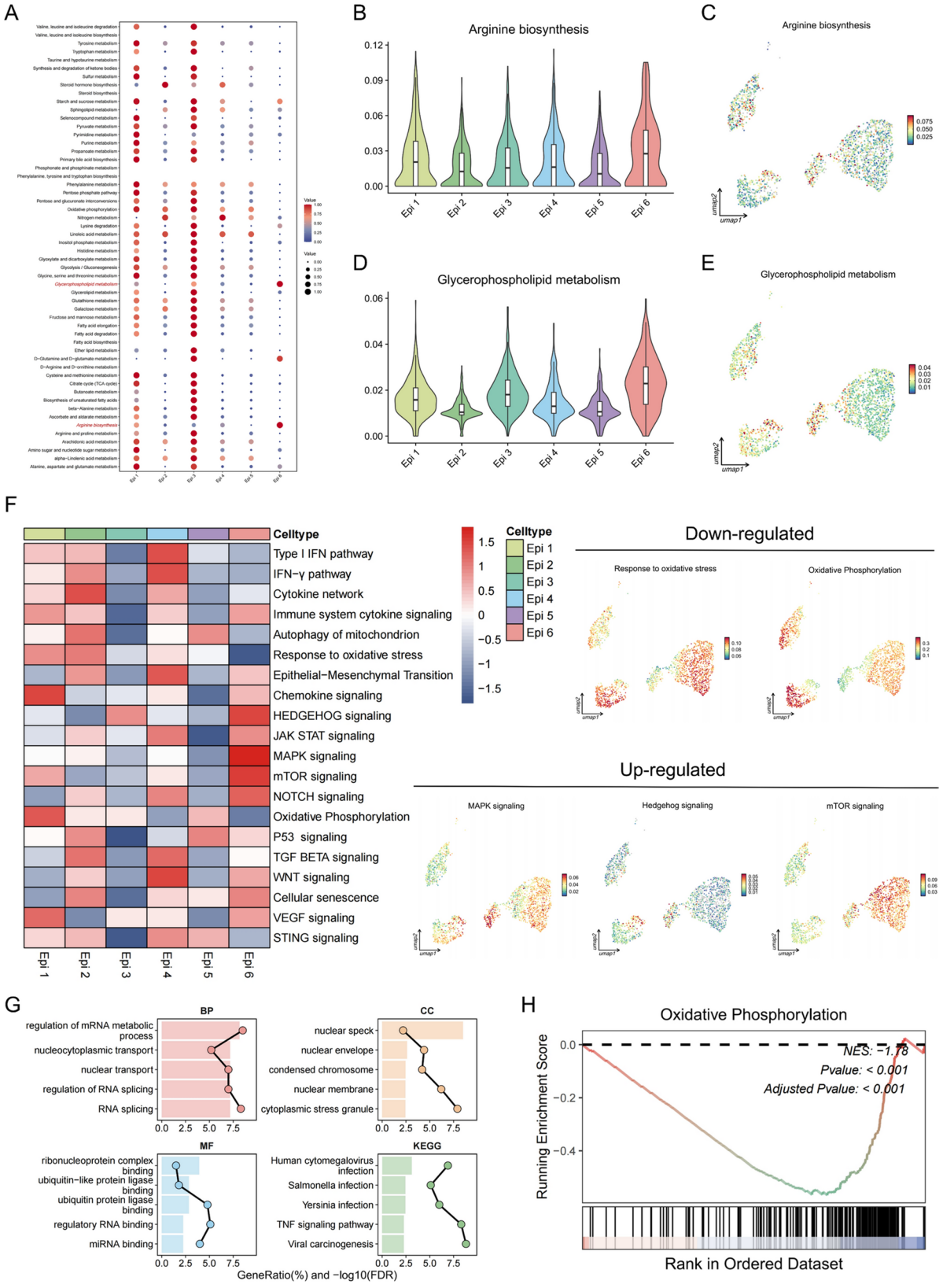

Fig. 4 Metabolic and functional activation landscape of the Epi 6 subgroup (**A**) Activity index of metabolic pathways among epithelial cell populations (**B**) Differences in the activity of arginine biosynthesis (**C**) Landscape of arginine biosynthesis (**D**) Differences in the activity of glycerophospholipid metabolism (**E**) Landscape of glycerophospholipid metabolism (**F**) Differences in epithelial cell populations across certain cancer-related pathways (**G**) GO and KEGG-based enrichment analysis of differentially expressed genes related to Epi 6 (**H**) GSEA of Epi 6

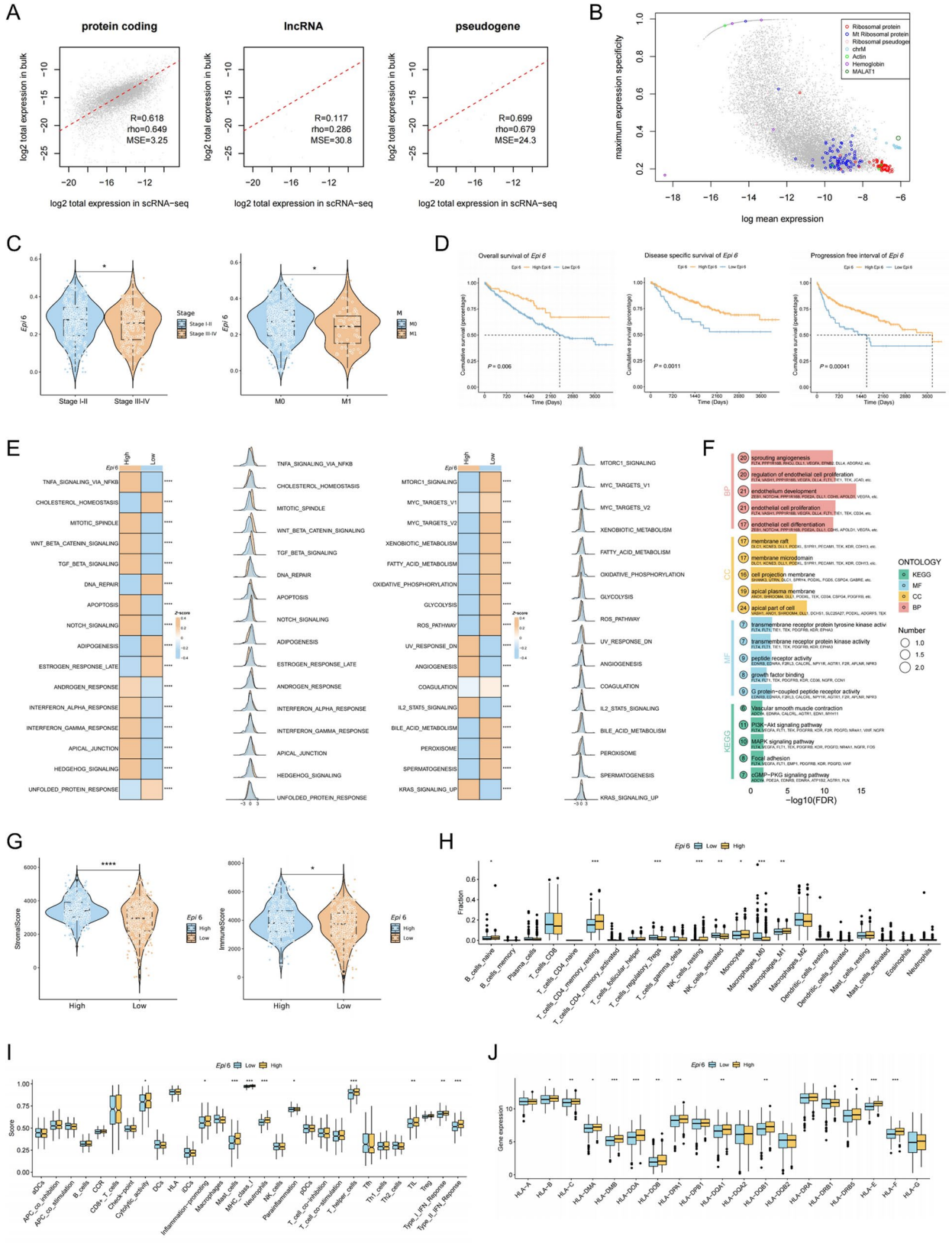

Fig. 5 (See legend on next page.)

(See figure on previous page.)

Fig. 5 Bulk transcriptome analysis of Epi 6 characteristics (**A**) Correlation of gene expression between bulk RNA and scRNA-seq (**B**) Noise-generating genes were removed during BayesPrism deconvolution (**C**) Differences in Epi 6 infiltration across clinical stages (**D**) Differences in prognosis between high and low Epi 6 infiltration groups (**E**) Differences in Hallmark pathway activation (**F**) Enrichment analysis of differentially expressed genes between high and low Epi 6 infiltration groups (**G**) Differences in stromal score and immune score (**H**) Differences in Cibersort immune cell abundance (**I**) Differences in HLA molecules expression

group had more M1 macrophages, while the low Epi 6 infiltration group had more Tregs (Fig. 5H). Among the immune-related pathways assessed by ssGSEA, those with statistical significance were all upregulated in the high Epi 6 infiltration group, such as T helper cells and interferon response (Fig. 5I). Additionally, most HLA molecules were also upregulated in the high Epi 6 infiltration group, including but not limited to HLA class I molecules (Fig. 5J).

Construction of Epi 6-related ccRCC prognostic model

Given that Epi 6 exhibited the strongest triaptosis activity in epithelial cell subpopulations in the aforementioned analysis, and was highly correlated with renal cell carcinoma traits and patient prognosis, we decided to construct a prognosis model for ccRCC patients based on Epi 6 feature genes, bridging single-cell omics heterogeneity with clinical decision-making. The hdWGCNA algorithm was used to extract key gene modules (Fig. 6A), yielding nine modules (Fig. 6B). We calculated activity scores based on the top 25 genes in each module (Fig. 6C), and it was evident that the yellow module was most closely associated with Epi 6 (Fig. 6D). We then performed an enrichment analysis on the genes in the yellow module using the Metascape portal to explore the biological significance of the module (Fig. 6E-F). Overall, entries related to RNA processing were significantly enriched, including but not limited to RNA splicing, spliceosomal complex assembly, and the mRNA surveillance pathway, suggesting that the genes in this module may be deeply involved in the entire process of RNA metabolism. The yellow module was therefore selected for subsequent prognostic model construction.

Given the large number of genes in the modules, we first performed preliminary screening using univariate Cox regression and Lasso regression, identifying nine key genes. Subsequently, based on these nine key genes, we integrated ten machine learning algorithms to construct a combined prognostic model. Ultimately, the StepCox[backward] + RSF model was identified as the optimal model due to its highest average C-index, incorporating four genes: RORA, SLC25A37, PKHD1, and PNISR (Fig. 7A). We thus obtained a risk score named Triaptosis-Epi 6 Score (TES). Scatter plots showed that as the TES increased, patient survival time decreased (Fig. 7B), while KM curves further illustrated significant prognostic stratification between high and low TES groups (Fig. 7C). The predictive ability of TES for patient survival was also assessed using ROC curves, with AUC values exceeding 0.9 in the TCGA-KIRC cohort and generally exceeding 0.7 in the E-MTAB-1980 and GSE167573 cohorts, even surpassing 0.8 in some cases (Fig. 7D). Given that the RSF model is a black-box model based on random forests, we used SurvSHAP(t) to assess the contribution of each model gene to prognostic assessment over time (Fig. 7E-F). The results showed that RORA was the most significant factor, followed by PKHD1, both of which are protective factors. SLC25A37 and PNISR are risk factors, with SLC25A37 having a greater predictive contribution. In summary, we constructed a high-precision ccRCC prognostic model based on key genes related to Epi 6, and enhanced the transparency of the black-box model using SurvSHAP(t), thereby advancing the credibility of artificial intelligence in clinical practice.

Differences in immune infiltration and immunotherapy between high and low TES groups

The TES score we constructed based on the characteristic genes of the Epi 6 cell population with high Triaptosis activity demonstrated satisfactory prognostic stratification capability. We then further explored the differences in immune function activation between the high and low TES groups to investigate the potential of TES to guide immunotherapy. The low TES group exhibited prominent monocyte infiltration, while the high TES group showed significantly increased Treg abundance (Fig. 8A). Interestingly, focusing on T cells, we found that the abundance of terminally exhausted T cells was increased in the high TES group (Fig. 8B), whereas in the low TES group, the majority of molecules in the TCR signaling pathway were upregulated (Fig. 8C). Additionally, molecules involved in antigen presentation, including but not limited to class I HLA, were largely upregulated in the low TES group (Fig. 8D). The upregulation of interleukin receptors, chemokine receptors, and TNF family molecules in the low TES group is also noteworthy (Fig. 8E-G). In summary, the low TES group is characterized by widespread immune function activation. This finding is also successfully reflected in the treatment response differences observed in the immunotherapy cohort. In Braun et al.'s ccRCC immunotherapy cohort, the CR/PR group had lower TES levels, and low TES was associated with better prognosis (Fig. 8H). The above analysis demonstrates the immunological significance of the TES prognostic model we constructed and its potential to guide the efficacy of immunotherapy.

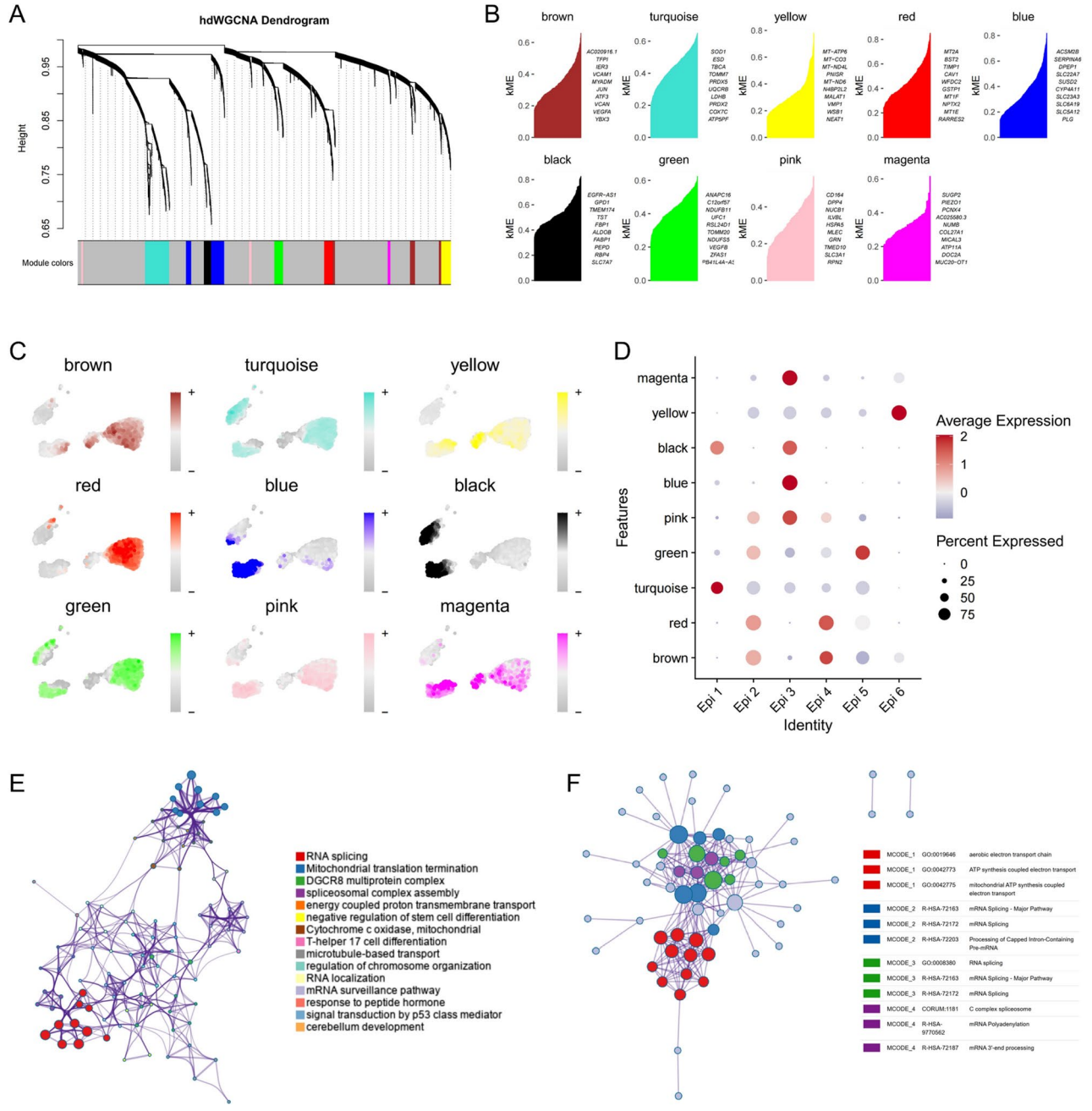

Fig. 6 hdWGCNA screening of key gene modules (**A**) hdWGCNA dendrogram (**B**) Key genes within the modules (**C**) Active distribution of the modules (**D**) Modular activity in different epithelial cell clusters (**E**) Metascape enrichment analysis based on the yellow module gene (**F**) Functional module protein interaction network based on the results of Metascape enrichment analysis of the yellow module gene

Differences in chemotherapy sensitivity between high- and low-TES groups

Based on GDSC2 data, we found that patients in the high TES group exhibited lower IC50 values for Gemcitabine, Cisplatin, Vorinostat, Rapamycin, and 5-FU (Fig. 9A), with significant negative correlations observed with TES levels (Fig. 9B). This suggests that patients in the high TES group may demonstrate greater sensitivity to these chemotherapeutic agents. Analyses utilizing the CTRP and PRISM databases further highlight that Gemcitabine may yield superior efficacy in high TES patients. Furthermore, the potential activity of Paclitaxel and Docetaxel in high TES patients should not be overlooked (Fig. 9C-F).

Characteristics of TES model component genes

We then returned to the single-cell transcriptome to characterize the expression patterns of genes composing the TES model. RORA exhibited the highest expression

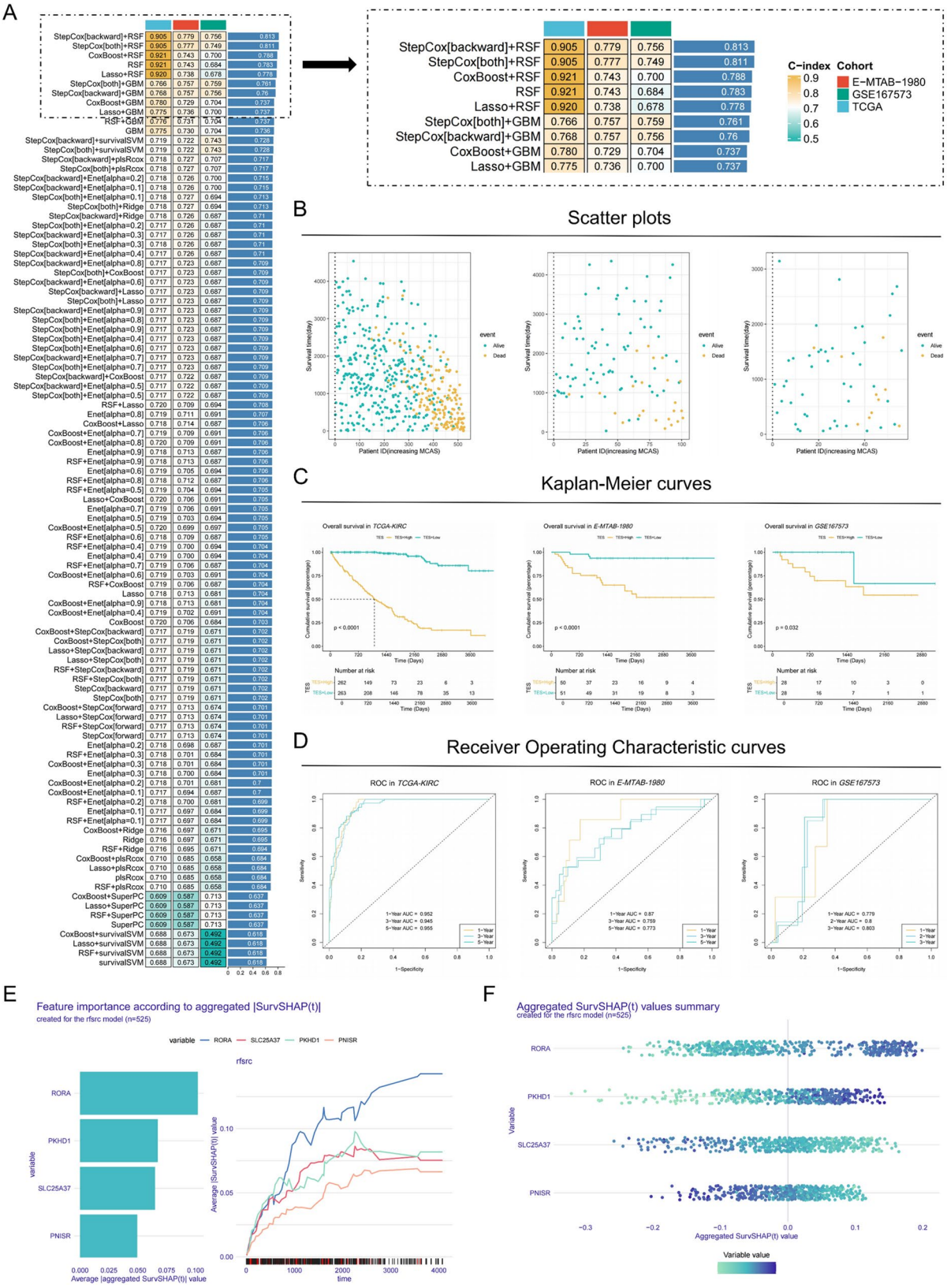

Fig. 7 Construction of machine learning prognostic model based on Epi 6 signature genes (**A**) C-index heatmap of different machine learning combination (**B**) Scatter plots of prognosis stratification (**C**) KM curves based on high and low TES (**D**) Time-dependent ROC curves of TES (**E**) Priority ranking of SurvSHAP(t) explanation (**F**) Beeswarm plot of SurvSHAP(t) explanation

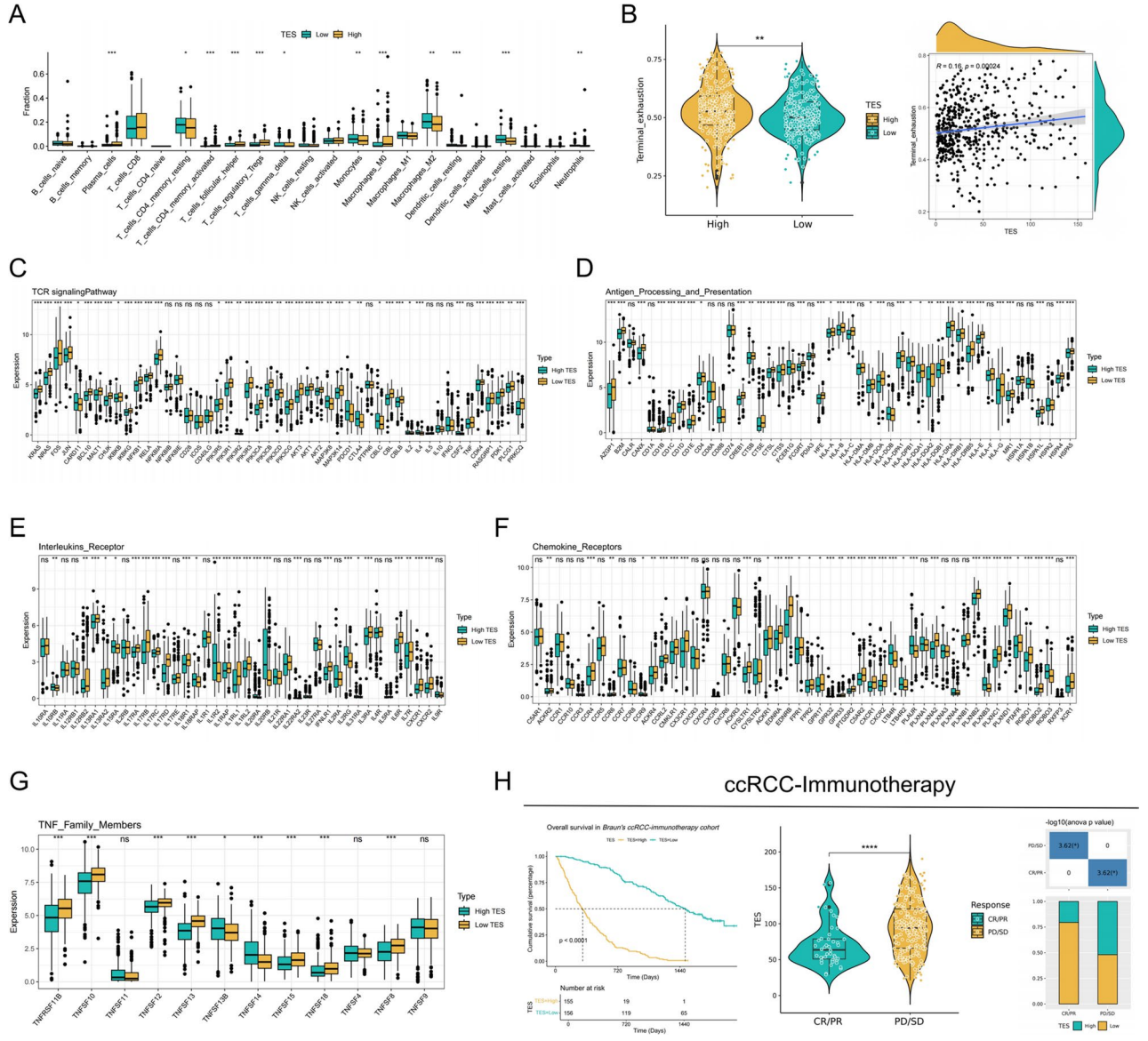

Fig. 8 Differences in immune functions between high- and low-TES groups (**A**) Differences in Cibersort immune cell infiltration (**B**) Differences in terminal exhausted T cell infiltration (**C**) Differential expression of genes in the TCR signaling pathway (**D**) Differential expression of genes in the antigen processing and presentation pathway (**E**) Differential expression of genes in the interleukins receptors (**F**) Differential expression of genes in the chemokine receptors (**G**) Differential expression of genes in the TNF family members (**H**) The guiding role of TES in Braun et al.'s immunotherapy cohort

in NK cells and T cells, with substantial expression also observed in epithelial cells, endothelial cells, and fibroblasts. PKHD1 expression demonstrated epithelial cell specificity. SLC25A37 showed the highest expression in monocytes, with significant expression also present in epithelial cells and endothelial cells. PNISR is highly expressed in various cell types (Fig. 10A-B). When focusing on epithelial cells, we found that all four model genes exhibited the highest expression levels in Epi 6 (Fig. 10C-D), consistent with the fact that our model is derived from the Epi 6-related gene module.

When we focus on specific clinical features, RORA expression was up-regulated in ccRCC samples and its high expression was associated with longer OS, DSS and PFI (Fig S3 A). PKHD1 expression was down-regulated in ccRCC and its high expression was also predictive of a better prognosis (Fig S3 B). SLC25A37 showed a typical oncogene profile and was up-regulated in ccRCC samples and those with high expression had a poorer prognosis (Fig S3 C). PNISR was upregulated in cancer tissues and associated with poorer OS, but stratification in DSS and PFI was not statistically significant (Fig S3 D). The above findings are consistent with the model explanation of SurvSHAP(t), further affirming the clinical relevance of our prognosis model. In addition, we conducted qRT-PCR experiments using ccRCC and normal

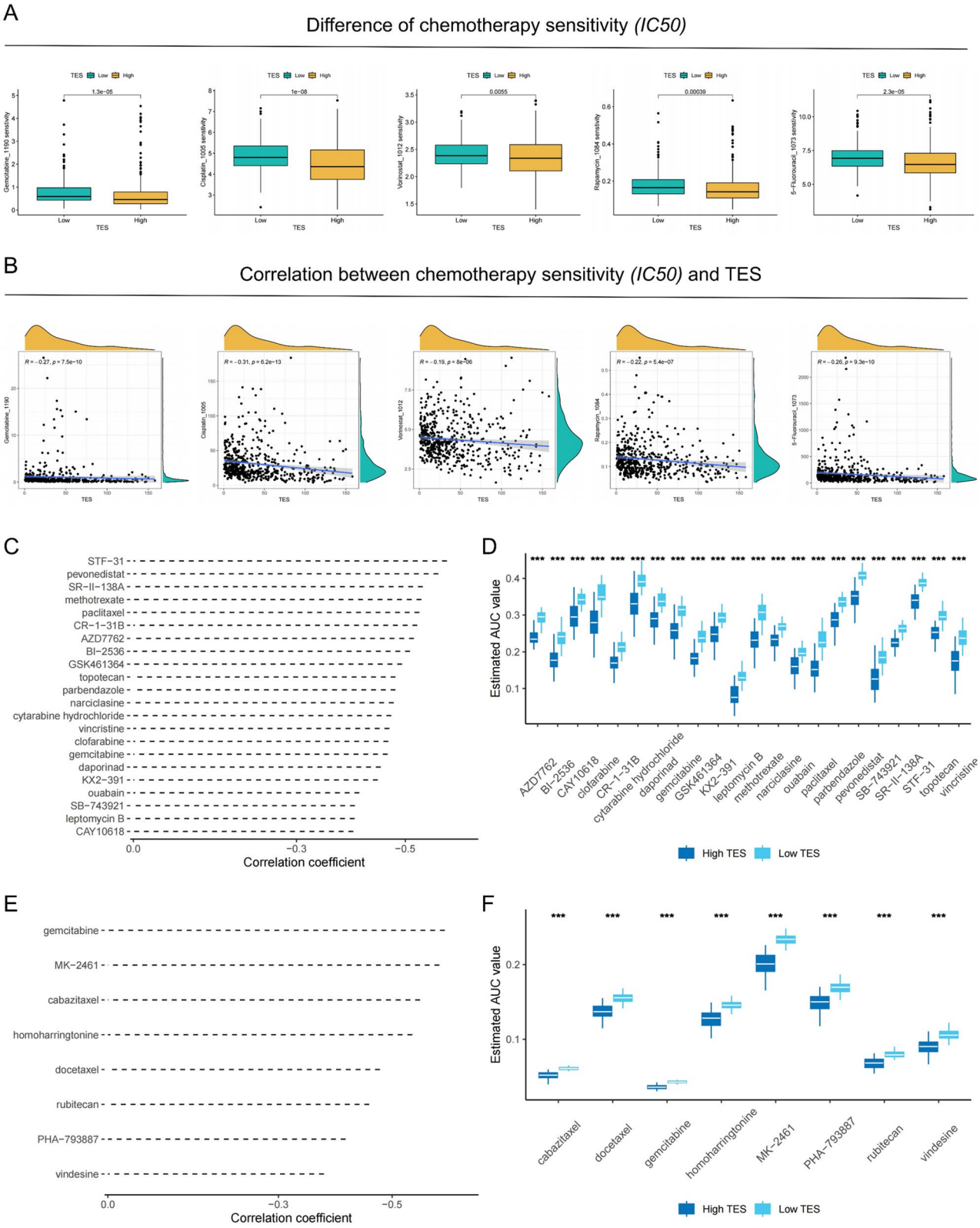

Fig. 9 The Chemotherapy Guidance Potential of TES (**A**) Differences in IC50 values for common chemotherapy drugs between High- and Low-TES groups (**B**) Correlation between IC50 and TES (**C**-**D**) Screening potential chemotherapeutic drugs based on CTRP (**E**-**F**) Screening potential chemotherapeutic drugs based on PRISM

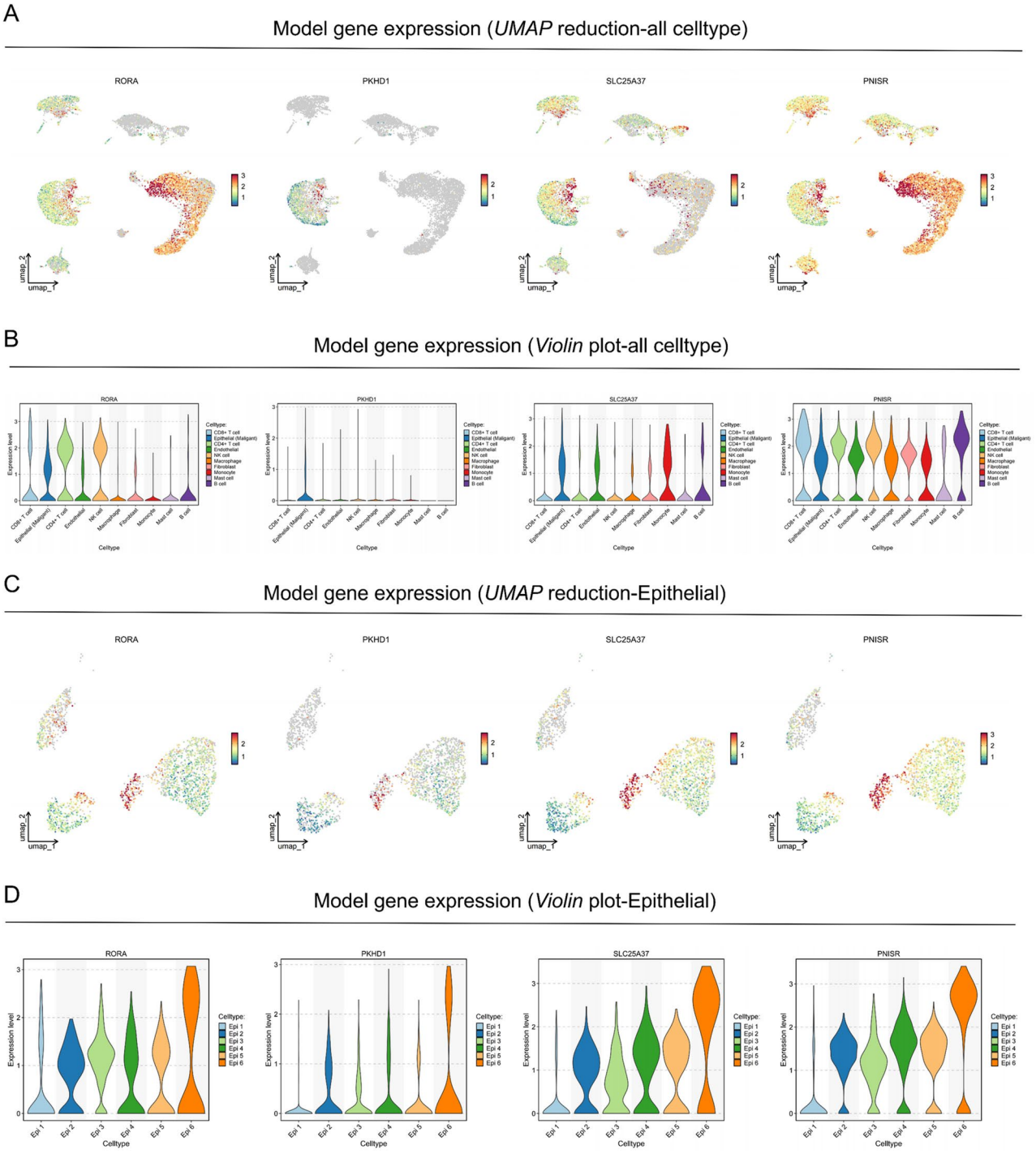

Fig. 10 Single-cell transcriptome expression characteristics of model genes (**A**) Expression patterns of model genes across all cell types (**B**) Comparison of model gene expression across all cell types (**C**) Expression patterns of model genes in epithelial (**D**) Comparison of model gene expression in epithelial

tissue samples to validate the differential expression of the genes identified in our model, and the results were consistent with our bioinformatics analysis (Fig. 11A). Immunohistochemical images from the HPA database further confirmed the differential expression patterns of these genes at the protein level (Fig. 11B). This lays the foundation for the future clinical application of our model.

Molecular drug development targeting the core oncogene SLC25A37 in the TES model

Given that SLC25A37 is the most prominent oncogene among the four model gene types, we attempted to screen drugs targeting SLC25A37 to lay the foundation for future drug development. Using the DSigDB database within the Enrichr portal, we identified the top four molecularly targeted drugs for SLC25A37. Molecular docking validation revealed Yohimbic acid demonstrated the highest binding potential with a binding energy of -9.2 kcal/mol (Fig. 12A), followed by Diacetylmorphine at -8.6 kcal/mol (Fig. 12B). Although the binding energies of Chlorpyrifos oxon and Methazolamide were less ideal than the aforementioned two, both were still below −6 kcal/mol (Fig. 12C-D). Subsequently, we performed molecular dynamics simulations on the most promising drug-target pair, Yohimbic acid and SLC25A37, to enhance credibility.

The stability of the simulated system was assessed using root mean square deviation (RMSD). The complex system exhibited stable fluctuations between 25 ns and 65 ns, showing a slight upward trend after 65 ns, but overall remained below 2.3 Å (Fig. 12E). Therefore, this small molecule demonstrates high stability when bound to the target protein. The radius of gyration (Rg) characterizes overall structural changes and reflects protein packing density. The complex system exhibited slight fluctuations during motion, indicating conformational changes in the small molecule-target protein complex (Fig. 12F).

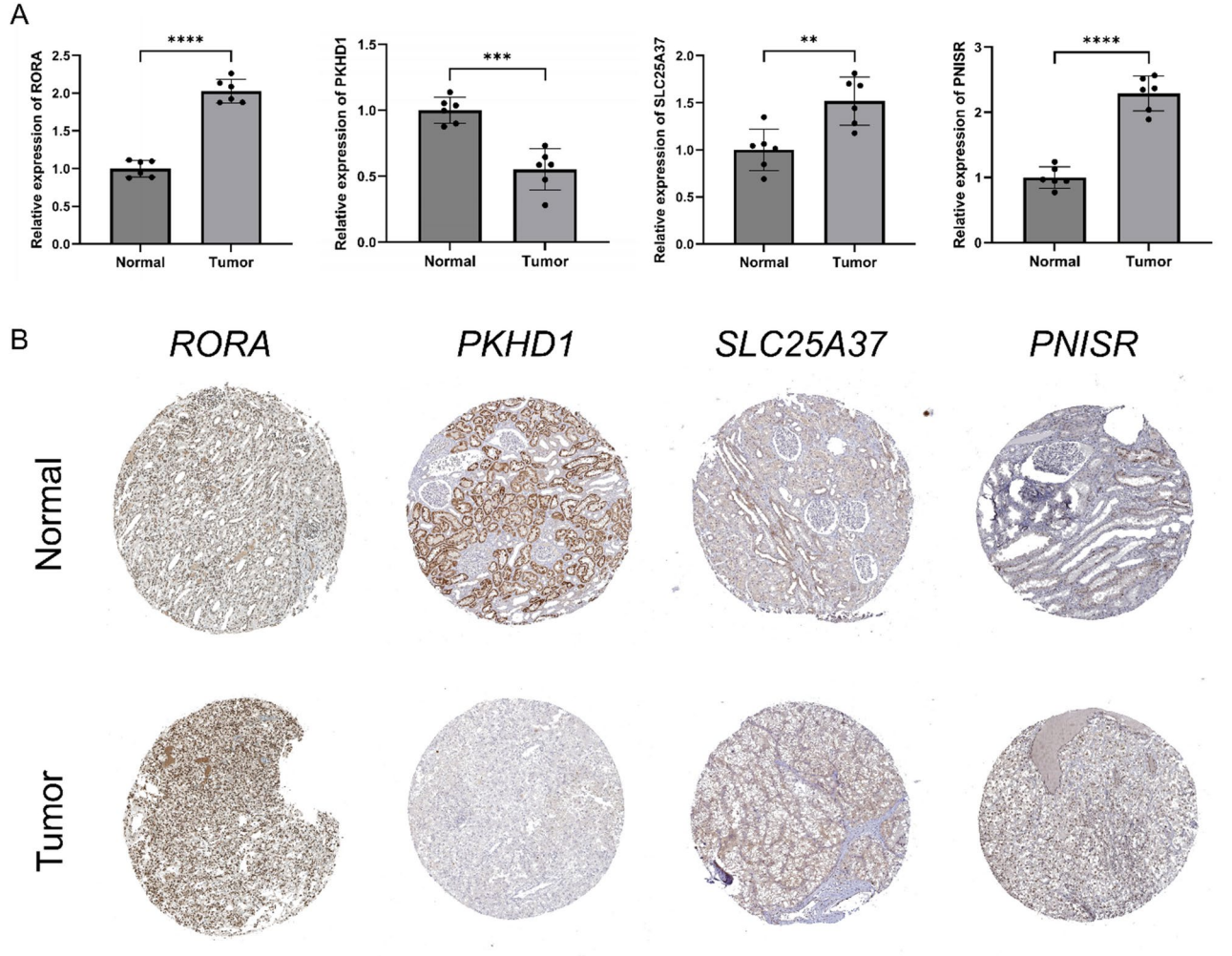

Fig. 11 Validation of differential expression of model genes (**A**) qRT-PCR validation of the differential expression of model genes (**B**) Immunohistochemical images of protein expression in model genes

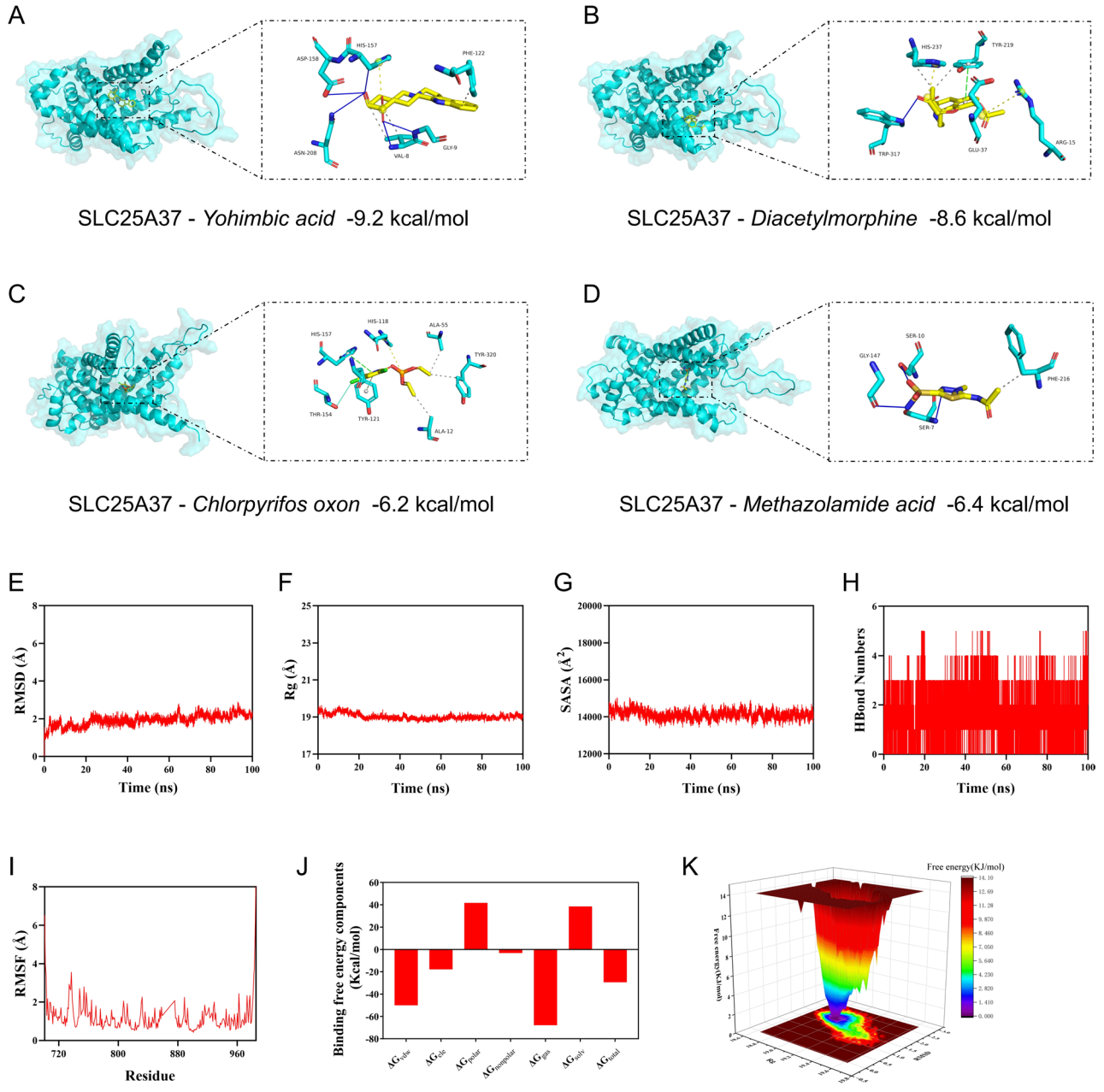

Fig. 12 Molecular drug screening targeting SLC25A37 (**A**-**D**) Molecular docking of potential small molecule drugs with SLC11A1 (**E**) RMSD values of protein-ligand complexes over time (**F**) Rg values of protein-ligand complexes over time (**G**) SASA values of protein-ligand complexes over time (**H**) Number of hydrogen bonds (**I**) RMSF values of amino acid backbone atoms in protein-ligand complexes (**J**) Binding free energy components (**K**) Free energy landscape of protein-ligand complexes

Solvent-accessible surface area (SASA), a measure of protein surface area, showed minor fluctuations in the complex system. This demonstrates that the bound small molecule affects the binding microenvironment, leading to a certain degree of SASA change (Fig. 12G). Hydrogen bonds play a crucial role in ligand-protein interactions. In most cases, the complex formed approximately three hydrogen bonds (Fig. 12H). This indicates strong hydrogen bonding interactions between the ligand and target protein. Root mean square fluctuation (RMSF) quantifies the flexibility of amino acid residues within a protein. The RMSF values for this complex were relatively low (mostly below 2.1 Å), suggesting low flexibility and high stability (Fig. 12I). Subsequently, the MM/PBSA method was employed to calculate the binding free energy between the small molecule and the target protein based on the complex's binding conformation (Fig. 12J). The results yielded a very low negative value, indicating substantial binding potential. Finally, a free energy landscape plot was utilized to visualize the free energy distribution

calculated from RMSD and Rg during the protein-ligand molecular dynamics simulations (Fig. 12K). In summary, the complex system exhibits stable binding, and the complex demonstrates strong hydrogen bonding interactions. Consequently, the small molecule interacts effectively with the target protein.

Discussion

Menadione, a lipophilic vitamin K precursor, induces a unique cell death pathway termed triaptosis by oxidatively modifying phosphatidylinositol 3-kinase PIK3C3/VPS34. This process involves GSH depletion and enhanced ROS production, which oxidize specific cysteine residues on PIK3C3. Consequently, PI(3)P levels decrease, leading to endosomal dysfunction and ultimately triaptosis. This mechanism demonstrates how severe oxidative stress compromises organellar integrity and triggers specific cell death pathways. In our study, we conducted the first integrated multi-omics analysis of triaptosis heterogeneity in ccRCC, subsequently constructing a robust prognostic model based on signature module genes from key epithelial cell subpopulations exhibiting high triaptosis activity. Overall, we leveraged bioinformatics and machine learning modeling to bridge the gap between biology and medicine, providing insights for personalized approaches from cellular discovery to clinical translation.

An interesting finding is that monocytes and macrophages exhibit the strongest triaptosis activity. During phagocytosis, macrophages initiate "respiratory bursts", actively generating large amounts of ROS [25–26]. This implies their intracellular basal ROS levels are inherently elevated, frequently depleting the GSH system. Consequently, when exposed to additional stimuli such as inflammatory cytokines or menadione analogues, they more readily breach the oxidative stress threshold, reaching the critical point of GSH depletion and PIK3C3 oxidation. An interesting finding is that monocytes and macrophages exhibit the strongest triaptosis activity. When performing phagocytosis, macrophages initiate "respiratory bursts," actively generating large amounts of ROS. This implies their intracellular basal ROS levels are inherently elevated, frequently depleting the GSH system. Consequently, when exposed to additional stimuli such as inflammatory cytokines or menadione analogues, they more readily breach the oxidative stress threshold, reaching the critical point of GSH depletion and PIK3C3 oxidation. On the other hand, macrophages serve as dedicated "scavenger" cells, exhibiting highly active endocytosis and phagocytosis. All these membrane transport processes rely heavily on PI(3)P to ensure proper localization of endocytic vesicles [27]. Consequently, even a slight reduction in PI(3)P can profoundly disrupt macrophage homeostasis, rapidly causing the collapse of their endosomal system and thereby increasing susceptibility to triaptosis.

Another noteworthy phenomenon is the low differentiation potential of cells exhibiting high triaptosis activity. First, triaptosis signifies a distinct mode of cell death. It is widely accepted that a cell undergoing death cannot simultaneously differentiate efficiently—a principle established early on, particularly in the context of apoptosis [28]. High triaptosis activity indicates that cells have entered a death program, naturally losing their differentiation potential. Furthermore, membrane remodeling is a crucial step in cell differentiation. For instance, receptor downregulation requires endocytosis, while new surface markers necessitate vesicular transport to the membrane [29–30]. As a central regulator of membrane dynamics and signal transduction, the disruption of PI(3)P during triaptosis inevitably deals a severe blow to the differentiation process [31].

We observed more pronounced interactions between angiogenesis-related co-receptors and endothelial cells in macrophages and monocytes exhibiting high triaptosis activity. As previously noted, triaptosis is mediated to some extent by the massive accumulation of ROS due to decompensated ROS production. ROS is actually a key potential inducer of HIF-1 [32], which directly triggers angiogenesis, including the massive release of VEGF factors [33–34]. Furthermore, ROS surges are accompanied by marked upregulation of the NF-κB pathway [35], which is also notorious for stimulating angiogenesis [36]. Naturally, we have another hypothesis. PI(3)P is crucial for forming vesicular membrane structures and conducting endosomal sorting. When PI(3)P is depleted during triaptosis, normal vesicle maturation is disrupted. These vesicles fail to fuse with lysosomes for degradation and may also be unable to undergo exocytosis. This could lead to the accumulation of immature vesicles loaded with factors like VEGF within the cell. The membrane rupture accompanying triaptosis could then trigger massive release of these vesicles and their VEGF contents into the extracellular space. However, this remains a hypothesis. We plan to confirm it through immunofluorescence and electron microscopy studies to determine whether macrophages undergoing high triaptosis exhibit substantial accumulation of VEGF-positive vesicles.

In spatial transcriptomics samples, we observed that triaptosis activity diminishes with increasing distance from the tumor epithelial core, indicating that the tumor core exhibits more pronounced triaptosis processes. The tumor core region is the least vascularized area, facing the most severe hypoxia [37]. Under hypoxic conditions, the electron transport chain in cellular mitochondria becomes impaired, leading to increased electron leakage and massive ROS production [38], which in turn mediates vigorous triaptosis.

In epithelial cells, we observed that the Epi 6 subpopulation exhibited the most robust triaptosis activity, significantly surpassing other subpopulations. This subpopulation demonstrated pronounced metabolic reprogramming, characterized by widespread downregulation of the three major metabolic pathways and oxidative phosphorylation, yet showed upregulation of arginine biosynthesis and glycerophospholipid metabolism. Arginine serves as a precursor for polyamines [39], which possess antioxidant properties capable of stabilizing membrane structures and scavenging ROS [40]. Argininbiosynthesis partially counteracts the intense ROS response during triaptosis. Furthermore, the core mechanism of triaptosis involves the collapse of the endosomal membrane system due to PI(3)P depletion. Phospholipids form the foundation of all cell membranes. The integrity and function of endosomes, lysosomes, and even the plasma membrane depend on continuous glycerophospholipid synthesis and remodeling [41]. The activation of glycerophospholipid metabolism likely represents an emergency repair mechanism initiated by cells to counteract the extensive membrane damage and leakage triggered by triaptosis. Moreover, prior studies have demonstrated that glycerophospholipid metabolism and arginine biosynthesis mediated by the tumor suppressor gene BRCA1 constitute a metabolic reprogramming associated with favorable prognosis in breast cancer [42]. This finding is echoed in our research: after deconvoluting single-cell transcriptomes to bulk transcriptomes using BayesPrism, patients with high Epi 6 infiltration exhibited better prognosis.

MAPK pathway activity was also found to be upregulated in the Epi 6 subpopulation exhibiting high triaptosis. ROS can activate key components in the MAPK pathway—P38 signaling and JNK signaling—thereby triggering cell death [43–44]. Furthermore, reports indicate that vitamin K2 induces cancer cell death through ROS-mediated activation of the JNK/p38 MAPK pathway [45]. This mechanism parallels the upregulation of MAPK signaling in epithelial cells exhibiting high triaptosis activity, as triaptosis was initially thought to be triggered by precursors of vitamin K.

Extending to the bulk transcriptome, we found that patients with high Epi 6 infiltration also exhibited downregulation of numerous metabolic pathway activities, consistent with single-cell transcriptomics. Furthermore, we observed stronger immune activation in the high Epi 6 infiltration group, including enhanced interferon pathways and HLA class I molecule expression. This may offer a potential explanation for the improved prognosis observed in patients with high Epi 6 infiltration.

Epi 6 epithelial cell subpopulations drew our attention due to their strongest triaptosis activity and high prognostic relevance. We extracted their characteristic gene modules via hdWGCNA and constructed a robust prognostic model based on integrated machine learning. The combination of StepCox[backward] + RSF was identified as the optimal method due to its highest average C-index. We successfully calculated risk scores for each bulk transcriptome sample based on the four included genes—RORA, PKHD1, SLC25A37, and PNISR—naming this score TES. RORA, identified as a tumor suppressor in gastric and prostate cancers, is regulated by multiple non-coding RNAs, with its downregulation associated with poor prognosis [46–47]. PKHD1 has gained attention in colorectal cancer, where its mutations indicate unfavorable patient outcomes [48]. SLC25A37, a solute transporter regulating intracellular iron homeostasis, demonstrates prognostic significance in ccRCC as part of a NETosis-related prognostic model. Overexpression of SLC25A37 stimulates proliferation and migration in ccRCC cancer cells [49]. Finally, research on PNISR remains scarce, with reports indicating its interaction with circular RNAs to maintain latent Kaposi's sarcoma-associated herpesvirus infection [50]. In summary, the genes incorporated into our model are associated with cancer in multiple ways, reflecting the biological significance underlying the model.

Our TES scoring system also delineates the immune function landscape of patients. The high-TES group exhibits increased Treg infiltration, with Tregs promoting immune evasion and tumor metastasis in ccRCC [51]. In the low-TES group, numerous immune killing pathway molecules show upregulation, such as TCR signaling and antigen presentation processes. Immune activation in the low-TES cohort was further demonstrated in the immunotherapy cohort, where patients with lower TES scores exhibited better prognosis and constituted the majority of CR/PR responders. Additionally, our model showed significant potential in guiding chemotherapy selection. We identified a series of chemotherapeutic agents potentially more effective for high-TES patients, notably Gemcitabine. In summary, beyond prognostic stratification, our TES score holds considerable promise for clinical treatment decisions.

The gene SLC25A37 in our model drew our attention due to its strong association with poor prognosis. We screened potential drugs targeting SLC25A37 and conducted molecular docking and molecular dynamics simulations. Results indicate that yohimbic acid exhibits satisfactory targeting capability for SLC25A37. Previous studies indicate that yohimbine plays a significant role in treating oral cancer [52–53]. Furthermore, it may exert anticancer effects by targeting oncogenes such as ERK and PIK3α [54]. Our chemoinformatics simulations lay the groundwork for subsequent targeted drug development and propose personalized insights into repurposing yohimbine as an old drug for new applications. Although

we are currently constrained by funding and experimental limitations, we have proposed a feasible plan for future experiments targeting SLC25A37 using yohimbic acid. First, to validate the anticancer efficacy of yohimbic acid, we plan to integrate in vitro cell experiments with in vivo animal studies. We intend to use at least two ccRCC cell lines, establishing control and Yohimbic acid gradient concentration groups, and assess the proliferative capacity of ccRCC cells using CCK-8 assays and colony formation assays. Additionally, we will use Transwell assays and wound healing assays to evaluate the effects of Yohimbic acid on the migration of ccRCC cells. For in vivo animal experiments, we plan to establish a subcutaneous xenograft tumor model in nude mice, again dividing the subjects into an experimental group and a group receiving varying concentrations of yohimbic acid. Tumor volume and weight will serve as primary outcome measures, and Ki-67 immunohistochemical staining of tumor tissue sections will be performed as an adjunctive assay for proliferation markers. The second part of the study aims to validate that yohimbic acid exerts anticancer effects by targeting SLC25A37. To verify target binding and direct interactions, we can employ surface plasmon resonance (SPR) or microcalorimetry (MST), which are the gold standards for demonstrating direct binding between small molecules and purified proteins. We can use purified SLC25A37 protein or fragments of its key transmembrane domains to measure the binding affinity between yohimbic acid and the protein. Additionally, we can employ cell-based thermal shift assay (CETSA) by treating cells or cell lysates with yohimbic acid and then heating them to denature the proteins. If the drug binds to SLC25A37, it will increase the protein's thermal stability. We will use Western blotting to detect the remaining levels of SLC25A37 in lysates at different temperatures. Rescue experiments provide key evidence that the anticancer activity of yohimbic acid is indeed SLC25A37-dependent. We plan to design four cell line groups: a control group (empty vector + solvent); a drug-treated group (empty vector + yohimbic acid); an SLC25A37 overexpression group (SLC25A37 overexpression plasmid + solvent); and the SLC25A37 overexpression + drug group (SLC25A37 overexpression plasmid + yohimbic acid). If yohimbic acid exerts its effects by inhibiting SLC25A37, then the anticancer effect of yohimbic acid should be significantly reversed in cells overexpressing SLC25A37. I believe that the further experimental studies described above will provide valuable insights into innovative targeted therapies for ccRCC.

Although our findings are encouraging, we must acknowledge several limitations. Fortunately, however, in this era of rapid progress in bioinformatics-based cancer research, many influential papers provide guidance for overcoming these limitations in the future [55–57]. First, our study is based on bioinformatics analysis, which may differ from actual biological expression. Moving forward, we will collaborate with laboratory partners to explore the significance of the triaptosis process in ccRCC cancer cells through extensive cellular experiments. Additionally, our bulk transcriptomics samples primarily focus on European and American populations, which may introduce ethnic biases. In the future, we plan to collect more bulk transcriptomics cohorts for more comprehensive analysis and establish a ccRCC cohort within our hospital to advance the development of our model reagent kit.

Supplementary Information

The online version contains supplementary material available at https://doi.org/10.1186/s40246-026-00982-3.

Supplementary Material 1.

Acknowledgements

The first author Haojie Dai would like to express his sincere gratitude to Yuqi Pan for her support and encouragement during Haojie Dai's busy academic schedule. Miss Pan's tenderness is always a source of the sweetest happiness. I would also like to congratulate Miss Pan on her acceptance onto the Global Health Management programme at Imperial College London. I miss you.

Author contributions

HD: Conceptualization, Bioinformatic analysis, Data curation, Writing. RL: Experiments, Writing. MZ: Writing. ZH and KJ: Conceptualization, Writing. CQ and KJ: Conceptualization, Funding acquisition, Writing. All authors reviewed the manuscript and approved it for publication.

Funding

This work was supported by Wannan Medical College teaching hospital research project (WK2024JXYY044), Changzhou Longcheng Medical Star Recommendation Project for Young Medical Sci-Tech Talents (lcyx2025010) and The Project Supported by Science Foundation of Kangda College of Nanjing Medical University (KD2024KYJJ274).

Data availability

The core data underpinning this study's conclusions are freely available in public repositories, notably the IEU Open GWAS (https://gwas.mrcieu.ac.uk/), TCGA (https://xenabrowser.net/) and GEO datasets (https://www.ncbi.nlm.nih.gov/geo/). In addition, other specific data can be requested from the corresponding author as reasonably required.

Code availability

The specific analysis codes will be available at https://github.com/Haojie-Dai/KIRC-Triaptosis.

Declarations

Ethics approval and consent to participate

Not applicable.

Consent for publication

Not applicable.

Competing interests

The authors declare no competing interests.

Received: 3 February 2026 / Accepted: 29 April 2026
Published online: 07 May 2026

References

1. Jonasch E, Walker CL, Rathmell WK. Clear cell renal cell carcinoma ontogeny and mechanisms of lethality. Nat Rev Nephrol. 2021;17(4):245–61.
2. Siegel RL, Miller KD, Fuchs HE, Jemal A. Cancer statistics, 2022. CA Cancer J Clin. 2022;72(1):7–33.
3. Hirata H, Hinoda Y, Ueno K, Nakajima K, Ishii N, Dahiya R. MicroRNA-1826 directly targets beta-catenin (CTNNB1) and MEK1 (MAP2K1) in VHL-inactivated renal cancer. Carcinogenesis. 2012;33(3):501–8.
4. Wilhelm M, Veltman JA, Olshen AB, Jain AN, Moore DH, Presti JC Jr, Kovacs G, Waldman FM. Array-based comparative genomic hybridization for the differential diagnosis of renal cell cancer. Cancer Res. 2002;62(4):957–60.
5. Hemal AK, Kumar A, Kumar R, Wadhwa P, Seth A, Gupta NP. Laparoscopic versus open radical nephrectomy for large renal tumors: a long-term prospective comparison. J Urol. 2007;177(3):862–6.
6. Chaffer CL, Weinberg RA. A perspective on cancer cell metastasis. Science. 2011;331(6024):1559–64.
7. Dai X, Wang D, Zhang J. Programmed cell death, redox imbalance, and cancer therapeutics. Apoptosis. 2021;26(7–8):385–414.
8. Galluzzi L, Vitale I, Aaronson SA, et al. Molecular mechanisms of cell death: recommendations of the Nomenclature Committee on Cell Death 2018. Cell Death Differ. 2018;25(3):486–541.
9. Peng F, Liao M, Qin R, Zhu S, Peng C, Fu L, Chen Y, Han B. Regulated cell death (RCD) in cancer: key pathways and targeted therapies. Signal Transduct Target Ther. 2022;7(1):286.
10. Swamynathan MM, Kuang S, Watrud KE, Doherty MR, Gineste C, Mathew G, Gong GQ, Cox H, Cheng E, Reiss D, Kendall J, Ghosh D, Reczek CR, Zhao X, Herzka T, Špokaitė S, Dessus AN, Kim ST, Klingbeil O, Liu J, Nowak DG, Alsudani H, Wee TL, Park Y, Minicozzi F, Rivera K, Almeida AS, Chang K, Chakrabarty RP, Wilkinson JE, Gimotty PA, Diermeier SD, Egeblad M, Vakoc CR, Locasale JW, Chandel NS, Janowitz T, Hicks JB, Wigler M, Pappin DJ, Williams RL, Cifani P, Tuveson DA, Laporte J, Trotman LC. Dietary pro-oxidant therapy by a vitamin K precursor targets PI 3-kinase VPS34 function. Science. 2024;386(6720):eadk9167.
11. Tang D, Kang R, Kroemer G. Triaptosis: an endosome-dependent cell death modality. Cell Res. 2025;35(4):237–8.
12. Yu Z, Lu W, Su C, Lv Y, Ye Y, Guo B, Liu D, Yan H, Mi H, Li T, Zhang Q, Cheng J, Mo Z. Single-Cell RNA-seq Identification of the Cellular Molecular Characteristics of Sporadic Bilateral Clear Cell Renal Cell Carcinoma. Front Oncol. 2021;11:659251.
13. Meylan M, Petitprez F, Becht E, Bougoüin A, Pupier G, Calvez A, Giglioli I, Verkarre V, Lacroix G, Verneau J, Sun CM, Laurent-Puig P, Vano YA, Elaïdi R, Méjean A, Sanchez-Salas R, Barret E, Cathelineau X, Oudard S, Reynaud CA, de Reyniès A, Sautès-Fridman C, Fridman WH. Tertiary lymphoid structures generate and propagate anti-tumor antibody-producing plasma cells in renal cell cancer. Immunity. 2022;55(3):527–e5415.
14. Sun G, Chen J, Liang J, Yin X, Zhang M, Yao J, He N, Armstrong CM, Zheng L, Zhang X, Zhu S, Sun X, Yang X, Zhao W, Liao B, Pan X, Nie L, Yang L, Chen Y, Zhao J, Zhang H, Dai J, Shen Y, Liu J, Huang R, Liu J, Wang Z, Ni Y, Wei Q, Li X, Zhou Q, Huang H, Liu Z, Shen P, Chen N, Zeng H. Integrated exome and RNA sequencing of TFE3-translocation renal cell carcinoma. Nat Commun. 2021;12(1):5262.
15. Braun DA, Hou Y, Bakouny Z, Ficial M, Sant' Angelo M, Forman J, Ross-Macdonald P, Berger AC, Jegede OA, Elagina L, Steinharter J, Sun M, Wind-Rotolo M, Pignon JC, Cherniack AD, Lichtenstein L, Neuberg D, Catalano P, Freeman GJ, Sharpe AH, McDermott DF, Van Allen EM, Signoretti S, Wu CJ, Shukla SA, Choueiri TK. Interplay of somatic alterations and immune infiltration modulates response to PD-1 blockade in advanced clear cell renal cell carcinoma. Nat Med. 2020;26(6):909–18.
16. Xie J, Zhang M, Qi M. Integrating Machine Learning Algorithms to Construct a Triaptosis-Related Prognostic Model in Melanoma. Cancer Manag Res. 2025;17:1127–41.
17. Ma RY, Black A, Qian BZ. Macrophage diversity in cancer revisited in the era of single-cell omics. Trends Immunol. 2022;43(7):546–63.
18. Zhang L, Li Z, Skrzypczynska KM, Fang Q, Zhang W, O'Brien SA, He Y, Wang L, Zhang Q, Kim A, Gao R, Orf J, Wang T, Sawant D, Kang J, Bhatt D, Lu D, Li CM, Rapaport AS, Perez K, Ye Y, Wang S, Hu X, Ren X, Ouyang W, Shen Z, Egen JG, Zhang Z, Yu X. Single-Cell Analyses Inform Mechanisms of Myeloid-Targeted Therapies in Colon Cancer. Cell. 2020;181(2):442–e45929.
19. Ma Y, Deng C, Zhou Y, Zhang Y, Qiu F, Jiang D, Zheng G, Li J, Shuai J, Zhang Y, Yang J, Su J. Polygenic regression uncovers trait-relevant cellular contexts through pathway activation transformation of single-cell RNA sequencing data. Cell Genom. 2023;3(9):100383.
20. Chu T, Wang Z, Pe'er D, Danko CG. Cell type and gene expression deconvolution with BayesPrism enables Bayesian integrative analysis across bulk and single-cell RNA sequencing in oncology. Nat Cancer. 2022;3(4):505–17.
21. Cable DM, Murray E, Zou LS, Goeva A, Macosko EZ, Chen F, Irizarry RA. Robust decomposition of cell type mixtures in spatial transcriptomics. Nat Biotechnol. 2022;40(4):517–26.
22. Liu Z, Liu L, Weng S, Guo C, Dang Q, Xu H, Wang L, Lu T, Zhang Y, Sun Z, Han X. Machine learning-based integration develops an immune-derived lncRNA signature for improving outcomes in colorectal cancer. Nat Commun. 2022;13(1):816.
23. Spytek M, Krzyziński M, Langbein SH, Baniecki H, Wright MN, Biecek P. survex: an R package for explaining machine learning survival models. Bioinformatics. 2023;39(12):btad723.
24. Newman AM, Liu CL, Green MR, Gentles AJ, Feng W, Xu Y, Hoang CD, Diehn M, Alizadeh AA. Robust enumeration of cell subsets from tissue expression profiles. Nat Methods. 2015;12(5):453–7.
25. Forman HJ, Torres M. Reactive oxygen species and cell signaling: respiratory burst in macrophage signaling. Am J Respir Crit Care Med. 2002;166(12 Pt 2):S4–8.
26. Iles KE, Forman HJ. Macrophage signaling and respiratory burst. Immunol Res. 2002;26(1–3):95–105.
27. Lee MF, Trotman LC. PTEN: Bridging Endocytosis and Signaling. Cold Spring Harb Perspect Med. 2020;10(10):a036103.
28. Cotter TG, Lennon SV, Glynn JG, Martin SJ. Cell death via apoptosis and its relationship to growth, development and differentiation of both tumour and normal cells. Anticancer Res. 1990 Sep-Oct;10(5A):1153–9.
29. Al-Awqati Q, Vijayakumar S, Takito J. Terminal differentiation of epithelia. Biol Chem. 2003;384(9):1255–8.
30. Xiang Z, Li J, Xu Y, Xu C, Zheng S, Chen J, Wei X, Xu X. Cell differentiation-related signaling pathways in hepatocellular carcinoma metastasis. Cancer Lett. 2025;627:217846.
31. Catimel B, Kapp E, Yin MX, Gregory M, Wong LS, Condron M, Church N, Kershaw N, Holmes AB, Burgess AW. The PI(3)P interactome from a colon cancer cell. J Proteom. 2013;82:35–51.
32. Belaidi E, Morand J, Gras E, Pépin JL, Godin-Ribuot D. Targeting the ROS-HIF-1-endothelin axis as a therapeutic approach for the treatment of obstructive sleep apnea-related cardiovascular complications. Pharmacol Ther. 2016;168:1–11.
33. Manuelli V, Pecorari C, Filomeni G, Zito E. Regulation of redox signaling in HIF-1-dependent tumor angiogenesis. FEBS J. 2022;289(18):5413–25.
34. Pezzuto A, Carico E. Role of HIF-1 in Cancer Progression: Novel Insights. A Review. Curr Mol Med. 2018;18(6):343–51.
35. Brandl N, Seitz R, Sendtner N, Müller M, Gülow K. Living on the Edge: ROS Homeostasis in Cancer Cells and Its Potential as a Therapeutic Target. Antioxid (Basel). 2025;14(8):1002.
36. Jiang Y, Zhang J, Shi C, Li X, Jiang Y, Mao R. NF-κB: a mediator that promotes or inhibits angiogenesis in human diseases? Expert Rev Mol Med. 2023;25:e25.
37. Lappano R, Todd LA, Stanic M, Cai Q, Maggiolini M, Marincola F, Pietrobon V. Multifaceted Interplay between Hormones, Growth Factors and Hypoxia in the Tumor Microenvironment. Cancers (Basel). 2022;14(3):539.
38. Ravi, Singh J. Redox imbalance and hypoxia-inducible factors: a multifaceted crosstalk. FEBS J. 2025;292(15):3833–48.
39. Fung TS, Ryu KW, Thompson CB. Arginine: at the crossroads of nitrogen metabolism. EMBO J. 2025;44(5):1275–93.
40. Liu JH, Wang W, Wu H, Gong X, Moriguchi T. Polyamines function in stress tolerance: from synthesis to regulation. Front Plant Sci. 2015;6:827.
41. Dolce V, Cappello AR, Lappano R, Maggiolini M. Glycerophospholipid synthesis as a novel drug target against cancer. Curr Mol Pharmacol. 2011;4(3):167–75.
42. Lucaora T, Morvan D. Joint Metabolomics and Transcriptomics Reveal Rewired Glycerophospholipid and Arginine Metabolism as Components of BRCA1-Induced Metabolic Reprogramming in Breast Cancer Cells. Metabolites. 2025;15(8):534.
43. Tormos AM, Taléns-Visconti R, Nebreda AR, Sastre J. p38 MAPK: a dual role in hepatocyte proliferation through reactive oxygen species. Free Radic Res. 2013;47(11):905–16.
44. Yang CB, Pei WJ, Zhao J, Cheng YY, Zheng XH, Rong JH. Bornyl caffeate induces apoptosis in human breast cancer MCF-7 cells via the ROS- and JNK-mediated pathways. Acta Pharmacol Sin. 2014;35(1):113–23.

45. Duan F, Yu Y, Guan R, Xu Z, Liang H, Hong L. Vitamin K2 Induces Mitochondria-Related Apoptosis in Human Bladder Cancer Cells via ROS and JNK/p38 MAPK Signal Pathways. PLoS ONE. 2016;11(8):e0161886.
46. Du C, Liang S, Wang X, Qi Y, Li S, Li H. EBV-miR-BART5-5p regulates RORA to promote proliferation and migration of gastric cancer cells. PLoS ONE. 2025;20(7):e0327323.
47. Li Y, He J, Yu L, Yang Q, Du J, Chen Y, Tang W. Hsa-miR-1290 is associated with stemness and invasiveness in prostate cancer cell lines by targeting RORA. Andrologia. 2022;54(5):e14396.
48. Han L, Gong F, Wu X, Tang W, Bao H, Wang Y, Wang D, Sun Y, Li P. Comprehensive characterization of PKHD1 mutation in human colon cancer. Cancer Med. 2024;13(1):e6796.
49. Mao X, Huang W, Xue Q, Zhang X. Prognostic impact and immunotherapeutic implications of NETosis-related prognostic model in clear cell renal cell carcinoma. J Cancer Res Clin Oncol. 2024;150(5):278.
50. Tagawa T, Oh D, Dremel S, Mahesh G, Koparde VN, Duncan G, Andresson T, Ziegelbauer JM. A virus-induced circular RNA maintains latent infection of Kaposi's sarcoma herpesvirus. Proc Natl Acad Sci U S A. 2023;120(6):e2212864120.
51. Li Z, Ma J, Xu M, Duan Y, Huang C, Dai Q, Yang Z. Regulatory T cells in renal cell carcinoma: tumor-promoting mechanisms and emerging therapeutic strategies. Int Immunopharmacol. 2025;163:115322.
52. Jabir NR, Khan MS, Alafaleq NO, Naz H, Ahmed BA. Anticancer potential of yohimbine in drug-resistant oral cancer KB-ChR-8-5 cells. Mol Biol Rep. 2022;49(10):9565–73.
53. Jabir NR, Tabrez S, Altwaijry N, Khan MS, Ramu AK, Ahmed BA. Estimating Anticancer Effects of Yohimbine in DMBA-Induced Oral Carcinogenesis Hamster Model: Utilizing Biochemical and Immunohistochemical Techniques. Cell Biochem Funct. 2024;42(7):e4132.
54. Jabir NR, Rehman MT, AlAjmi MF, Ahmed BA, Tabrez S. Prioritization of bioactive compounds envisaging yohimbine as a multi targeted anticancer agent: insight from molecular docking and molecular dynamics simulation. J Biomol Struct Dyn. 2023;41(20):10463–77.
55. Xia W, Liu J, Chen R, Feng J, Wu L, Wang Y, Wang X, Song C, Mao W. Molecular subtypes and prognostic signature rooted in disulfidptosis highlight tumor microenvironment in lung adenocarcinoma. Chin J Cancer Res. 2025;37(5):796–820.
56. Gong Z, Du M, Li Y, Ye B, Huang Y, Gong H, Wang W, Chen L, Ding Z, Zhang P. Machine learning identifies TIME subtypes linking EGFR mutations and immune states in lung adenocarcinoma. NPJ Digit Med. 2025;8(1):796.
57. Zhang P, Liang X, Ye B, Wang X, Wang Y, Gong Z, Huang Y, Liu J, Huang C, Luo P. Metabolic reprogramming signature predicts immunotherapy efficacy in lung adenocarcinoma: Targeting SLC25A1 to overcome immune resistance. Chin J Cancer Res. 2025;37(6):1000–19.

Publisher's Note